The Astrophysical Journal, 958:97 (19pp), 2023 November 20 https://doi.org/10.3847/1538-4357/acfedc

Predicting the Radiation Field of Molecular Clouds Using Denoising Diffusion Probabilistic Models

Duo Xu[1], Stella S. R. Offner[2], Robert Gutermuth[3], Michael Y. Grudić[4], Dávid Guszejnov[5], and Philip F. Hopkins[6]
[1] Department of Astronomy, University of Virginia, Charlottesville, VA 22904-4235, USA; xuduo117@virginia.edu
[2] Department of Astronomy, The University of Texas at Austin, Austin, TX 78712, USA
[3] Department of Astronomy, University of Massachusetts, Amherst, MA 01003, USA
[4] Carnegie Observatories, 813 Santa Barbara St., Pasadena, CA 91101, USA
[5] Center for Astrophysics | Harvard & Smithsonian, 60 Garden St., Cambridge, MA 02138, USA
[6] TAPIR, Mailcode 350-17, California Institute of Technology, Pasadena, CA 91125, USA
Received 2023 July 31; revised 2023 September 11; accepted 2023 September 28; published 2023 November 15

Abstract

Accurately quantifying the impact of radiation feedback in star formation is challenging. To address this complex problem, we employ deep-learning techniques known as denoising diffusion probabilistic models (DDPMs) to predict the interstellar radiation field (ISRF) strength based on three-band dust emission at 4.5, 24, and 250 μm. We adopt magnetohydrodynamic simulations from the STARFORGE project that model star formation and giant molecular cloud (GMC) evolution. We generate synthetic dust emission maps matching observed spectral energy distributions in the Monoceros R2 (MonR2) GMC. We train DDPMs to estimate the ISRF using synthetic three-band dust emission. The dispersion between the predictions and true values is within a factor of 0.1 for the test set. We extended our assessment of the diffusion model to include new simulations with varying physical parameters. While there is a consistent offset observed in these out-of-distribution simulations, the model effectively constrains the relative intensity to within a factor of 2. Meanwhile, our analysis reveals a weak correlation between the ISRF solely derived from dust temperature and the actual ISRF. We apply our trained model to predict the ISRF in MonR2, revealing a correspondence between intense ISRF, bright sources, and high dust emission, confirming the model's ability to capture ISRF variations. Our model robustly predicts radiation feedback distribution, even in complex, poorly constrained ISRF environments like those influenced by nearby star clusters. However, precise ISRF predictions require an accurate training data set mirroring the target molecular cloud's unique physical conditions.

Unified Astronomy Thesaurus concepts: Interstellar medium (847); Interstellar dust (836); Interstellar radiation field (852); Astrostatistics (1882); Astrostatistics techniques (1886); Molecular clouds (1072); Magnetohydrodynamics (1964); Young stellar objects (1834)

1. Introduction

Stellar feedback plays a crucial role in the star formation process, manifesting in two main forms: mechanical feedback and radiative feedback (Fall et al. 2010; Girichidis et al. 2020). Mechanical feedback involves the injection of momentum and kinetic energy into the surrounding clouds through stellar winds, including protostellar outflows and isotropic stellar wind–driven bubbles (Arce et al. 2007; Churchwell et al. 2007; Frank et al. 2014). Conversely, radiative feedback is associated with the dissociation and ionization of cold molecular gas by the intense radiation emitted by massive stars (Walch et al. 2012; Grudić & Hopkins 2019; Rosen & Krumholz 2020). This radiation also exerts pressure on the surrounding gas and dust, resulting in the formation of ionized bubbles known as H II regions, which release a substantial amount of energy (Lopez et al. 2014).

Recent studies have highlighted the significant impact of stellar feedback on the star formation process. Simulations show that mechanical feedback, such as outflows and stellar winds, reduces protostellar masses and accretion rates and disperses surrounding gas, leading to a decrease in both the global star formation rate and efficiency (Matzner 2007; Federrath et al. 2014; Federrath 2015; Offner & Chaban 2017; Guszejnov et al. 2022). However, the energy injection from outflows is typically limited to smaller scales, ranging from subparsec to parsec scales (Wang et al. 2010; Xu et al. 2022a). In contrast, the combined effects of photoionization and radiation pressure from massive stars and their H II regions result in the heating of the surrounding gas and efficient dispersal of the nearby cloud (Dale et al. 2012, 2013). The radiation feedback from massive stars can have a broad impact, spanning scales from a few to tens of parsecs (Walch et al. 2012; Lopez et al. 2014; Rosen & Krumholz 2020; Grudić et al. 2022; Guszejnov et al. 2022; Rosen 2022).

In order to gain a comprehensive understanding of how stellar feedback influences the star formation process, including star formation rate and efficiency, it is crucial to study feedback mechanisms across molecular clouds with varying physical and chemical conditions. However, accurately quantifying the impact of radiation from massive stars continues to present a challenge in observational studies. There are several current "classical" approaches to estimating the radiation field from observations. For example, the strength of the radiation field originating from massive stars is commonly estimated using dust emission (Bernard et al. 2010). However, the mean dust temperature as derived from long-wavelength emission gives an incomplete picture of local conditions. Pound & Wolfire (2023) developed a framework using the ratio between

far-infrared (FIR) fine-structure lines, such as [O I], [C I], and [C II], to estimate the strength of the radiation field through photodissociation region (PDR) models. However, PDR models rely on simplified assumptions about the cloud geometry and density distribution, leading to uncertainties when applied to actual observational data. This approach also does not provide an accurate estimate of the radiation field within the cloud due to young embedded sources. Other PDR codes, such as 3D-PDR (Bisbas et al. 2012), offer the advantage of allowing for arbitrary density distributions and the ability to specify radiating sources within the cloud, addressing some of the uncertainties mentioned earlier. However, degeneracy due to physical conditions imposes a significant limitation in using line ratios to determine the strength of the radiation field, since different number densities and radiation field strengths can produce the same line ratio (Pound & Wolfire 2023). Additionally, mapping FIR lines across molecular clouds is time-consuming, especially in quiescent regions, where [O I], [C I], and [C II] emission is relatively faint.

By comparison, machine learning provides a promising avenue for improving the estimation of physical variables given relatively limited observational data. There has been a proliferation in machine learning–based approaches to predict physical quantities from observational data across various fields, including solar physics (Asensio Ramos & Díaz Baso 2019), the interstellar medium (ISM; Peek & Burkhart 2019; Xu et al. 2020a, 2020b, 2022a, 2022b), and the realm of galaxies and cosmology (Wu & Boada 2019; Neutsch et al. 2022). Machine learning provides a powerful tool to study mechanical stellar feedback, as it enables complex morphological features, previously only detectable by visual inspection, to be identified quickly and reliably. Recent studies have developed and employed a deep-learning method called Convolutional Approach to Structure Identification to systematically identify protostellar outflows and wind-driven bubbles in nearby molecular clouds using molecular line data cubes (Van Oort et al. 2019; Xu et al. 2020a, 2020b, 2022a).

Recently, denoising diffusion probabilistic models (DDPMs) have emerged as powerful and reliable tools for image generation (Sohl-Dickstein et al. 2015; Ho et al. 2020) and have shown great potential in addressing prediction tasks within the field of astronomy. Smith et al. (2022) employed DDPMs to generate synthetic images resembling observed galaxies, achieving a high level of realism. In another study, Wang et al. (2023) utilized DDPMs to enhance image quality and suppress noise in interferometric observations. Furthermore, Xu et al. (2023) applied DDPMs to infer the number density of molecular clouds, a parameter notoriously challenging to measure based on readily obtainable column density maps. The DDPMs exhibit superior accuracy in predicting molecular cloud number density, underscoring their effectiveness and reliability in the estimation task.

In this paper, we employ a deep-learning approach based on DDPMs to estimate the radiation field strength induced by massive stars within molecular clouds. Specifically, we utilize multiple bands of dust emission to infer the radiation field strength. In Section 2, we elucidate the diffusion model utilized in our analysis and delineate the procedure employed to generate the training set from magnetohydrodynamic (MHD) simulations. Subsequently, in Section 3, we comprehensively evaluate the performance of our diffusion model in predicting the radiation field strength. Additionally, we apply our diffusion model to actual observational data, as detailed in Section 3. Finally, we consolidate our findings and draw conclusions in Section 4.

2. Data and Method

2.1. MHD Simulations

We employ MHD simulations acquired from the STAR FORmation in Gaseous Environments (STARFORGE) project (Grudić et al. 2021). The project introduces a novel numerical framework for conducting 3D radiation MHD simulations of star formation, allowing for a comprehensive examination of multiple processes. These processes encompass the formation, accretion, evolution, and dynamics of individual stars within massive giant molecular clouds (GMCs) while considering the intricate effects of stellar feedback. The stellar feedback mechanisms taken into account include jets, radiative heating and momentum, stellar winds, and supernovae.

The simulations in the STARFORGE project utilize the GIZMO code (Hopkins 2015), which incorporates the mesh-free Lagrangian MHD method. Specifically, the star cluster formation is simulated within a GMC characterized by an initial mass of $2 \times 10^4\ M_\odot$ and a radius of 10 pc (Grudić et al. 2022; Guszejnov et al. 2022). The initial magnetic field strength is set to 2 μG, and the cloud possesses an initial virial parameter of 2. The simulations achieve a mass resolution of $10^{-3}\ M_\odot$ and span an evolutionary time frame of approximately 9 Myr. The interstellar radiation field (ISRF) default configuration is scaled to the background spectral energy distribution (SED) of the solar neighborhood, with the Draine (1978) value of $G_0 = 1.7$ in the far-UV band. Additionally, we employ simulations where the ISRF is intensified by factors of 10 and 100, corresponding to $G_0 = 17$ and 170 (Guszejnov et al. 2022). This alternative setup enables us to assess the performance of the machine-learning model under stronger radiation field conditions. Significantly, the simulations account for stellar feedback by incorporating accretion- and fusion-powered stellar radiation in five distinct frequency bins. These bins include H-ionizing ($\lambda < 912$ Å), far-ultraviolet (912 Å $< \lambda <$ 1550 Å), near-ultraviolet (1550 Å $< \lambda <$ 3600 Å), optical–to–near-infrared (3600 Å $< \lambda < 3\ \mu$m), and FIR ($\lambda > 3\ \mu$m) ranges. It is important to highlight that our work incorporates simulations spanning different evolutionary stages ranging from 2 to 8 Myr. This wide temporal range encompasses both early and late stages of star formation, as well as the evolution of GMCs.

In addition to the full physics simulations, we incorporate a specific simulation that emphasizes the impact of stellar winds and radiation feedback while deactivating the presence of jets (Guszejnov et al. 2022). This alternative simulation configuration introduces slight variations in the physical setup and enhances the diversity of cloud morphologies within the simulations. By including this simulation in our analysis, we expand the range of training data and further enrich the training set for our machine-learning model. We provide a summary of the adopted simulations in Table 1. For further comprehensive information regarding the STARFORGE project, additional details can be found in Grudić et al. (2021).

Table 1
Summary of STARFORGE Simulations[a]

	t_s (Myr)	ISRF (G_0)	Jets	$N_{\rm sample}$
Training and testing	3.5–7.5	1.7	Yes	6750
	4–5.5	1.7	No	3000
Testing	5	17	Yes	81
	5	170	Yes	81
	1.7–4.3[b]	1.7	Yes	127

Notes.
[a] Evolutionary time, ISRF, whether protostellar jets are included, and the number of image samples.
[b] These simulations are initially subjected to turbulent driving for two crossing times, equivalent to 17.5 Myr. Furthermore, they incorporate the updated heating and cooling treatments.

2.2. MonR2 Observations

We adopt the Monoceros R2 (MonR2) GMC as an observational test case. It is well observed at all bandpasses of interest for this project. It is located 860 pc away, is 33,000 $M_\odot$, and hosts over 900 young stellar objects (YSOs) with excess IR emission indicative of dusty circumstellar material such as protoplanetary disks or protostellar envelopes (Pokhrel et al. 2020). Thus, our fiducial STARFORGE calculation provides a reasonable representation of the MonR2 region given its cloud mass, evolutionary stage, and level of star formation activity.

We adopt Spitzer Extended Solar Neighborhood Archive (Gutermuth et al., in preparation; Pokhrel et al. 2020) Spitzer (Werner et al. 2004) mosaics at 4.5 μm from the Infrared Array Camera (IRAC; Fazio et al. 2004) and 24 μm from the Mid-Infrared Photometer for Spitzer (MIPS; Rieke et al. 2004). For the 250 μm image, we use the Herschel (Pilbratt et al. 2010) Spectral and Photometric Imaging REceiver (SPIRE; Griffin et al. 2010) image from Pokhrel et al. (2016) that includes an absolute calibration correction to the Planck High Frequency Instrument (Planck HFI Core Team et al. 2011) data of the same region of sky.

The trained model as described in Section 2.3 operates on physical scales of 1/8 parsec pixel^{-1}, which translates to 30″ pixel^{-1} at MonR2's distance. For our analysis, we resample all three infrared images to a common pixel grid set by the IRAC 4.5 μm image, the highest-resolution data of the collection at 2.″2 beamwidth and 0.″87 pixel^{-1} size (MIPS 24 μm is 6.″3 beamwidth and 1.″8 pixel^{-1}; SPIRE 250 μm is 18″ beamwidth and 6″ pixel^{-1}). Since the beam resolutions of all three images are less than our final pixel scale, we simply box-average and down-sample the flux into the desired 30″ pixel^{-1} size grid. We then apply a mask to limit consideration to those pixels with coverage in all three bandpasses. The resulting coverage spans an area of 5.23 deg^2. This treatment was applied using standard routines for these tasks (e.g., *hastrom, hrebin*) from the IDL Astronomy User's Library (Landsman 1993).

2.3. Synthetic Dust Observations

To calculate the dust temperature and generate synthetic dust emission at multiple wavelengths, we employ the 3D radiative transfer code RADMC-3D (Dullemond et al. 2012). STARFORGE uses a subgrid model for protostellar evolution (Offner et al. 2009) and stores the luminosity, radius, and effective temperature of each source. Due to computational constraints, it is not feasible to assign a unique stellar spectrum to each individual star. Instead, we categorize the stars into four groups based on their effective temperature: <2000, 2000–5000, 5000–10,000, and >10,000 K. For each category, we calculate the mean effective temperature by considering the mean luminosity and surface area of the stars within that category. The calculation of the mean effective temperature is solely based on the stars that are located within the domain where the radiative transfer is conducted. An example of star categorization in one simulation snapshot is presented in Appendix A.

We explore two different approaches for modeling the stellar spectrum, specifically the SED, in our study: the blackbody SED and the YSO SED. The blackbody SED assumes a blackbody spectrum based on the mean effective temperature of the stars. However, circumstellar disks play a significant role in shaping the SEDs of young sources (Whitney et al. 2003; Robitaille et al. 2007; Offner et al. 2012). In the STARFORGE simulations, the formation of circumstellar disks is suppressed due to strong magnetic braking. The YSO SED accounts for the emission reprocessing (e.g., extinction, absorption and remission, scattering) caused by these (missing) disks. We adopt the stellar spectra with disks from Robitaille (2017). For each category of stars, we retrieve the SED from the table in Robitaille (2017) by selecting the one that closely matches the effective temperature and stellar radius of the star. The table also includes different inclination angles for young stars with disks. In our approach, we adopt the spectrum with an inclination angle that is closest to 45°.

In the radiative transfer calculation, we employ two different dust models depending on the gas number density. For gas number densities exceeding 10^5 cm^{-3}, we utilize the dust model proposed by Koepferl et al. (2017) for dense gas. This model consists of three dust compositions: 80.63% big grains (>200 Å), 13.51% very small grains (20–200 Å), and 5.86% ultrasmall grains (<20 Å) in the form of polycyclic aromatic hydrocarbon (PAH) molecules. On the other hand, for gas number densities below 10^5 cm^{-3}, we adopt the dust model developed by Hensley & Draine (2023) specifically designed for diffuse gas. This model incorporates two dust components: astrodust (90.69%) and PAH (9.31%). In Appendix B, we investigate various cutoffs on gas number densities when selecting dust models and explore different dust models. This exercise illustrates that the choice of dust model is crucial to reproduce the observed SEDs; our hybrid model reproduces the relative fluxes in the three bands significantly better than the canonical Draine & Lee (1984) model or either of the two models alone.

Dust heating in molecular clouds is influenced by multiple mechanisms, with radiation from stars and the ISRF playing dominant roles. It is important to mention that the simulation data used in this study do not include the saved dust temperature during the simulation runs. The gas temperature is not a good proxy for the dust temperature, as they differ by an order of magnitude in shocks and lower-density regions, where the dust and gas are not well coupled. Consequently, using the gas temperature in place of the dust temperature in the radiative transfer would result in a substantial difference in the calculated dust emission, spanning several orders of magnitude. To address this, we utilize the RADMC-3D package to calculate the dust temperature in postprocessing.

Given that GIZMO utilizes a Lagrangian meshless finite mass method rather than a Cartesian grid, we employ the *yt*

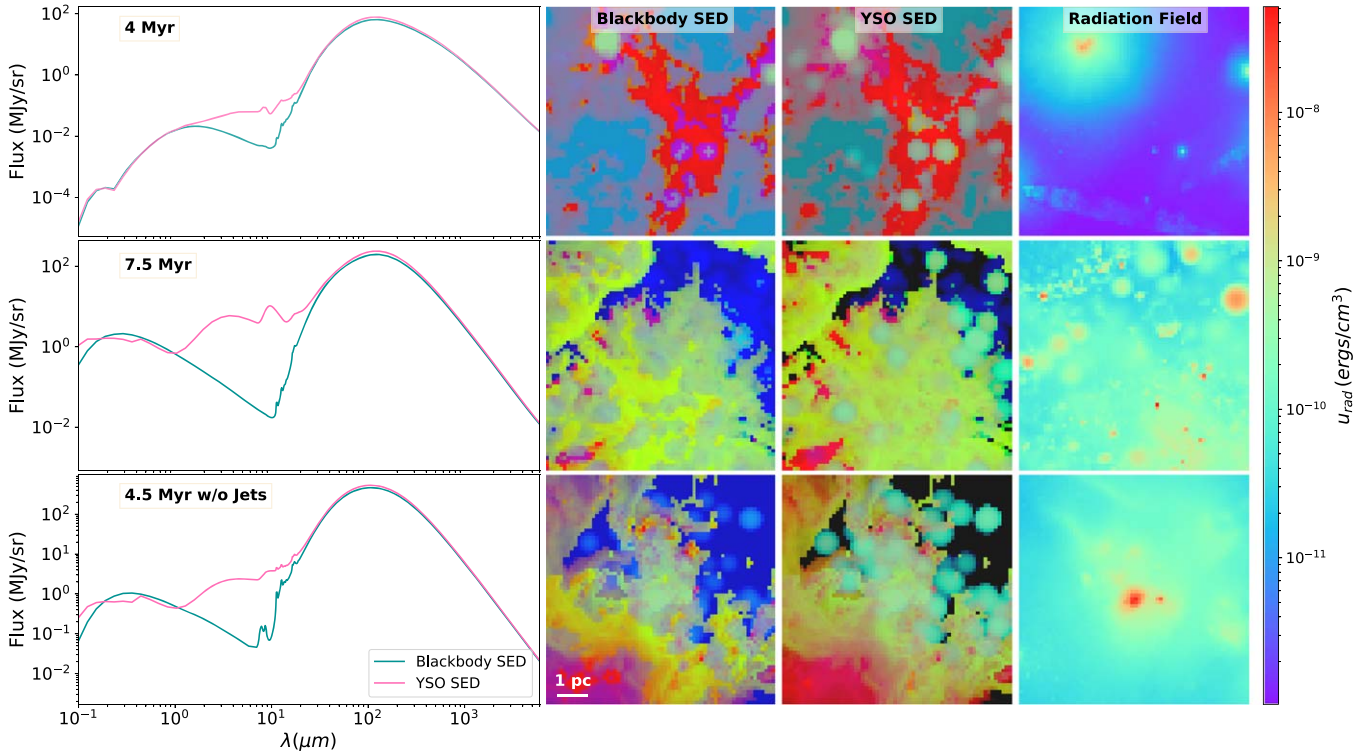

Figure 1. Synthetic dust observations, including images and SEDs, for simulations at various evolutionary stages and with different feedback configurations. The first column illustrates the SEDs of the synthetic observations. The second and third columns showcase the three-color synthetic dust images at 4.5 (blue), 24 (green), and 250 (red) μm wavelengths, utilizing different radiative transfer configurations. The fourth column presents the projected radiation field strength obtained from the simulations, measured in erg cm^{-3}.

toolkit (Turk et al. 2011) to sample the simulation data and transform it into a uniform Cartesian grid. We use these processed data as the input for RADMC-3D in our analysis. We assume a gas-to-dust ratio of 100 and incorporate the Henyey–Greenstein anisotropic scattering model in the radiative transfer calculation.

Due to computational constraints, we generate the synthetic dust images for each $10 \times 10 \times 10$ pc^3 box with an image resolution of 80×80 pixels. We verify that the radiative transfer results remain robust regardless of the resolution. In Appendix B, we present the radiative transfer simulations with a resolution of 256×256, and we show that the resulting SEDs are consistent with those obtained at lower resolutions.

To account for stars located near the box boundaries, we apply an additional postprocessing step. After generating the initial synthetic dust images with dimensions of 80×80 pixels, we crop a 1 pc boundary on all four sides of the image. This results in a final image size of 64×64 pixels, representing an 8×8 pc^2 sky area.

Figure 1 illustrates the synthetic dust emission at 4.5, 24, and 250 μm, considering the two different treatments for the stellar spectrum, a blackbody SED and a YSO SED, at various evolutionary stages. The figure also presents the projected radiation field averaged by the radiation energy along the line of sight. The synthetic dust emission SEDs are sensitive to the choice of stellar spectrum. The SEDs generated with blackbody SEDs as the radiating sources exhibit two distinct peaks, representing the contributions of stellar radiation in the optical–to–near-infrared range and dust emission of the cloud material in the mid-IR–to–FIR range. In contrast, the SEDs generated with the radiating sources modeled as YSOs display an infrared excess from 1 to 10 μm. This difference arises because the YSO SEDs exhibit higher levels of infrared emission due to emission reprocessing by the dust in circumstellar disks. We note that neither set of synthetic images exhibit outflow features, which often appear in these bands (Looney et al. 2007; Tobin et al. 2008; Takami et al. 2010). Some of the excess observed emission likely arises from shock-excited H_2 and CO lines (Cyganowski et al. 2008), which are not included in our radiative transfer modeling step.

2.4. Constructing the Training Set

In this study, we utilize three specific bands of dust emission, namely, 4.5, 24, and 250 μm, as input for training the machine-learning model to predict the radiation field at the pixel level. These bands cover both near-infrared and FIR dust emission and, importantly, encompass information that is well modeled by our training set. Figure 2 presents a gallery of SEDs for all of the synthetic data, with darker colors indicating a higher number of stacked SEDs. Observations from the MonR2 GMC are included in the figure for reference, showcasing the Spitzer (3.6, 4.5, 5.8, 8.0, and 24 μm) and Herschel (250, 350, and 500 μm) bands. The synthetic SEDs demonstrate a broad range of coverage for the observed data points. Nonetheless, there is an evident discrepancy in the synthetic SEDs, particularly in the 8 μm emission, where it is noticeably underestimated. This discrepancy is caused by strong PAH emission, indicating that the adopted dust model does not replicate the observed PAH emission adequately. Part of the discrepancy is likely due to the absence of nonthermal excitation mechanisms, such as shocks, which are not included in postprocessing. It is important to note that the presence of

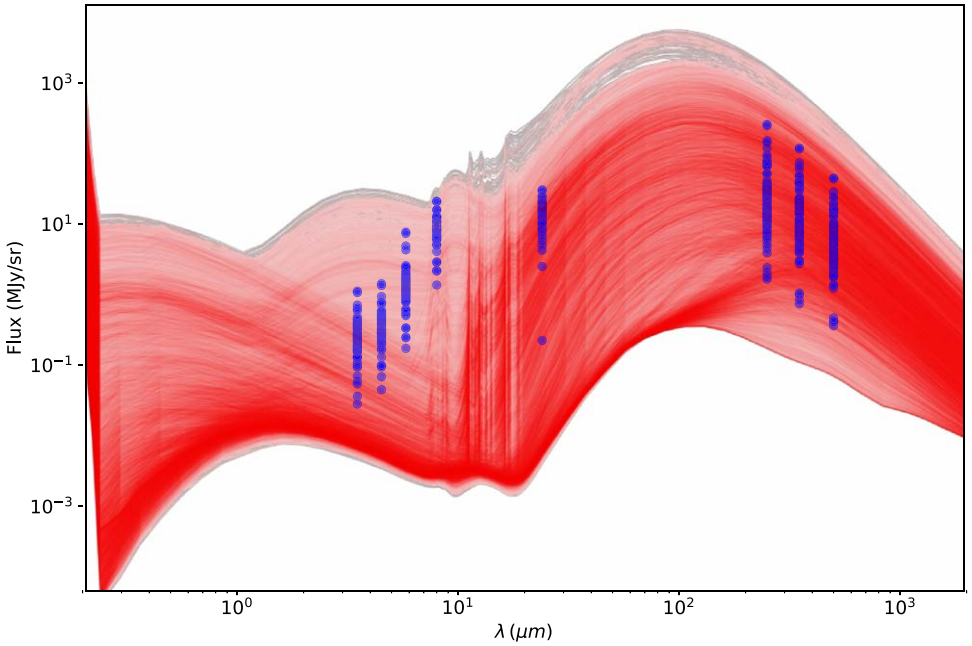

Figure 2. Collection of all of the synthetic dust SEDs, where the intensity of the color is proportional to the number of stacked SEDs. Blue dots represent observations in the Spitzer (3.5, 4.5, 5.8, 8.0, and 24 μm) and Herschel (250, 350, and 500 μm) bands within MonR2.

H_2 lines at 2.22, 2.41, 2.63, and 3.00 μm may cause contamination in the 3.6 μm bandpass. Additionally, the strong aromatic infrared bands at 3.30, 6.20, 7.70, 8.60, 11.30, and 12.70 μm can potentially contaminate the 3.6, 5.8, and 8 μm bands (Foschino et al. 2019). As our project aims to infer the ISRF using a limited amount of data, it is crucial to ensure that the synthetic data closely resemble the real data. To mitigate this issue and achieve better performance, we have excluded bandpasses that include H_2 lines and strong PAH feature emission (3.6, 5.8, and 8.0 μm) in this study.

To enhance the model's capability to handle real observational data, which may include the presence of foreground and background stars, we randomly introduce bright false sources that simulate such stars in the 4.5 μm images. These sources exhibit a 2D Gaussian intensity distribution, where the peak intensity is randomly selected as a fraction between 0.1 and 1 of the 99.5th percentile of the 4.5 μm images. For each synthetic dust map, we utilize the projected radiation field averaged along the line of sight, weighted by radiation energy, as the target for the machine-learning training. In summary, the input consists of three-band dust emission maps ($3 \times 64 \times 64$), while the target or model output is the corresponding projected radiation field (64×64).

We generate a total of 9750 synthetic dust maps encompassing various evolutionary stages, feedback configurations, and treatments for the stellar spectrum. To evaluate the performance of the machine-learning model, the data are randomly split into an 80% training set and a 20% test set.

To comprehensively assess the performance of the machine-learning model across different environments, we generate an additional 162 synthetic dust observations. These synthetic observations are generated from simulations with ISRF strengths of $G_0 = 17$ and 170. Importantly, these new synthetic dust observations are entirely distinct from the training data, allowing us to evaluate the model's performance on previously unseen data.

2.5. Denoising Diffusion Probabilistic Models

Diffusion models, also known as DDPMs, are state-of-the-art generative methods used in deep learning and computer vision research (Sohl-Dickstein et al. 2015; Ho et al. 2020; Rombach et al. 2022). These models leverage probability theory and stochastic processes to effectively model and reconstruct data, with a focus on modeling the conditional distribution of clean data given noisy observations. By estimating the underlying distribution of the data, DDPMs capture its statistical properties, patterns, variations, and complexities.

The primary objective of DDPMs is to denoise and reconstruct the original signal from noisy or corrupted data. By modeling the distribution of clean data and incorporating diffusion processes, DDPMs excel at recovering true underlying structure while suppressing noise. The diffusion process is a key component, governing the evolution of the data distribution over time.

The DDPM starts with a simple initial distribution and gradually transforms it into the target distribution, which represents the conditional distribution of clean data. This transformation occurs through a sequence of steps involving diffusion and denoising operations. Controlled noise is introduced during diffusion to guide the data along a diffusion path, followed by a denoising step that estimates the clean data from the noisy observations. Typically, deep neural network architectures like CNNs are employed in the denoising step, training them to map noisy observations to clean data. Figure 3 illustrates an example of the reverse process applied to our test data, demonstrating the gradual conversion of Gaussian noise into our desired target over 1000 time steps.

In our work, we adopt the same diffusion model described in Xu et al. (2023), where a detailed mathematical explanation of DDPM formulation is provided. To train our diffusion model for the task of reconstructing the radiation fields based

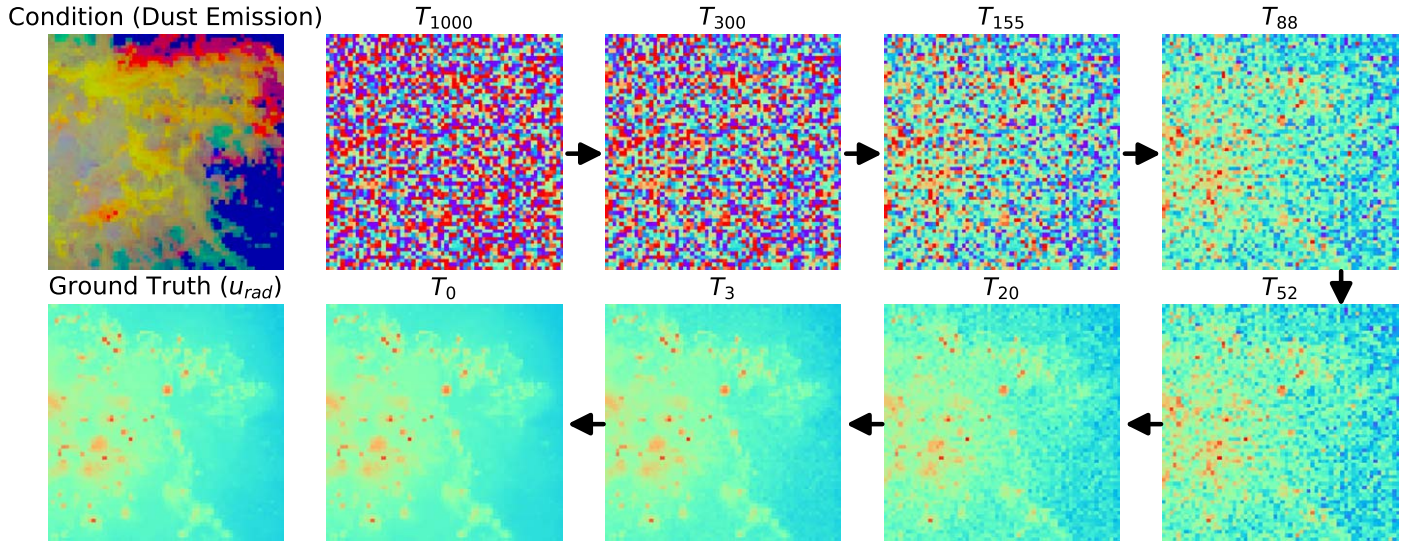

Figure 3. Demonstration of the diffusion process (reverse) on a sample in the test set. In the upper row, the first panel represents the input (condition) for the diffusion model, while in the lower row, the first panel represents the corresponding target (ground truth). The initial status is denoted as T_{1000}, which corresponds to the random Gaussian noise. The final states of the reverse Markov chain, representing the final predictions by the diffusion model, are indicated as T_0. The intermediate steps of the reverse Markov chain, ranging from $T = 0$ to 1000, are depicted in the remaining panels.

on three-band dust emission maps, we follow the training strategy outlined in Xu et al. (2023).

3. Results

3.1. Assessing the Performance of the Diffusion Model

In this section, we assess the performance of the diffusion model in predicting the radiation field strength based on the three-band dust emission. We begin by evaluating the diffusion model's performance on the test set. Figure 4 illustrates the predicted radiation field alongside the three-band dust emission and the ground-truth radiation field. By visual comparison, the diffusion model accurately predicts the radiation field at the pixel level.

To further evaluate the performance, we present a 2D histogram depicting the correlation between the diffusion model's predictions and the ground-truth values of the radiation fields in Figure 5. The histogram demonstrates a strong alignment between the diffusion model's predictions and the ground-truth radiation field values. The deviation between the true and predicted value is within a factor of 0.1. To provide a more interpretable representation of the radiation energy, we convert the radiation field energy into ISRF luminosity in the solar neighborhood. This conversion is achieved by adopting the mean intensity integrated over frequency from Mathis et al. (1983), where $4\pi J = 0.0217\ \mathrm{erg\ cm^{-2}\ s^{-1}}$.

We further investigate the comparison between the traditional approach, which estimates the ISRF from dust temperature, and the actual ISRF in the test set. Bernard et al. (2010) proposed an analytical formula to estimate the ISRF based on dust temperature in GMCs following a power law

$$\mathrm{ISRF_{T-Dust}} = \left(\frac{T_{\mathrm{Dust}}}{17.5\ \mathrm{K}}\right)^{4+\beta}, \quad (1)$$

where the dust emissivity index β is assumed to be 2, which is a good fit to our adopted dust model at long wavelengths. This equation follows from the balance of dust absorption and emission in the diffuse ISM, assuming an ambient ISRF with an SED like the ISRF in the solar neighborhood. Therefore, it should describe the low-extinction parts of the cloud fairly well but not the inner parts that are subject to extinction and irradiation by protostars.

Figure 6 depicts the correlation between the true ISRF and the dust temperature calculated using RADMC-3D. We observe a weak or even unclear linear trend between these two quantities. Since the plot is in log scale, the pattern appears similar to the $\mathrm{ISRF_{T-Dust}}$ versus $\mathrm{ISRF_{True}}$ plot but with different magnitudes in their values. For reference, the one-to-one line of $\mathrm{ISRF_{T-Dust}}$ and $\mathrm{ISRF_{True}}$ is also shown in Figure 6. The inferred ISRF from the dust temperature exhibits a notable offset from the true ISRF, mainly due to the extinction of radiation from stars within the cloud by dust along the line of sight. This offset diminishes at low ISRF values, where line-of-sight extinction is minimal. Overall, this highlights a significant level of uncertainty, with scatter and offset of over a factor of 10, in the traditional approach for estimating the ISRF from dust emission as compared to our machine-learning approach.

3.2. Testing on Out-of-distribution Data

Although the test set was not included in the training process, the synthetic dust observations in both the test set and the training set originate from the same sequence of MHD simulations. As a result, the diffusion model is potentially capable of learning all of the intricacies within the synthetic dust emission and achieving unfairly accurate predictions, which could be significantly less accurate when applied to more diverse data. To address the possible issue of overfitting, we evaluate the performance of the diffusion model on unseen data. This includes synthetic images created using different dust models and entirely novel MHD simulations featuring diverse physical parameters. Since simulations can never perfectly model observations, even when great care is taken to match the physical conditions and include relevant physical effects, our training data are, by definition, out of distribution compared to the observational data. The tests presented here

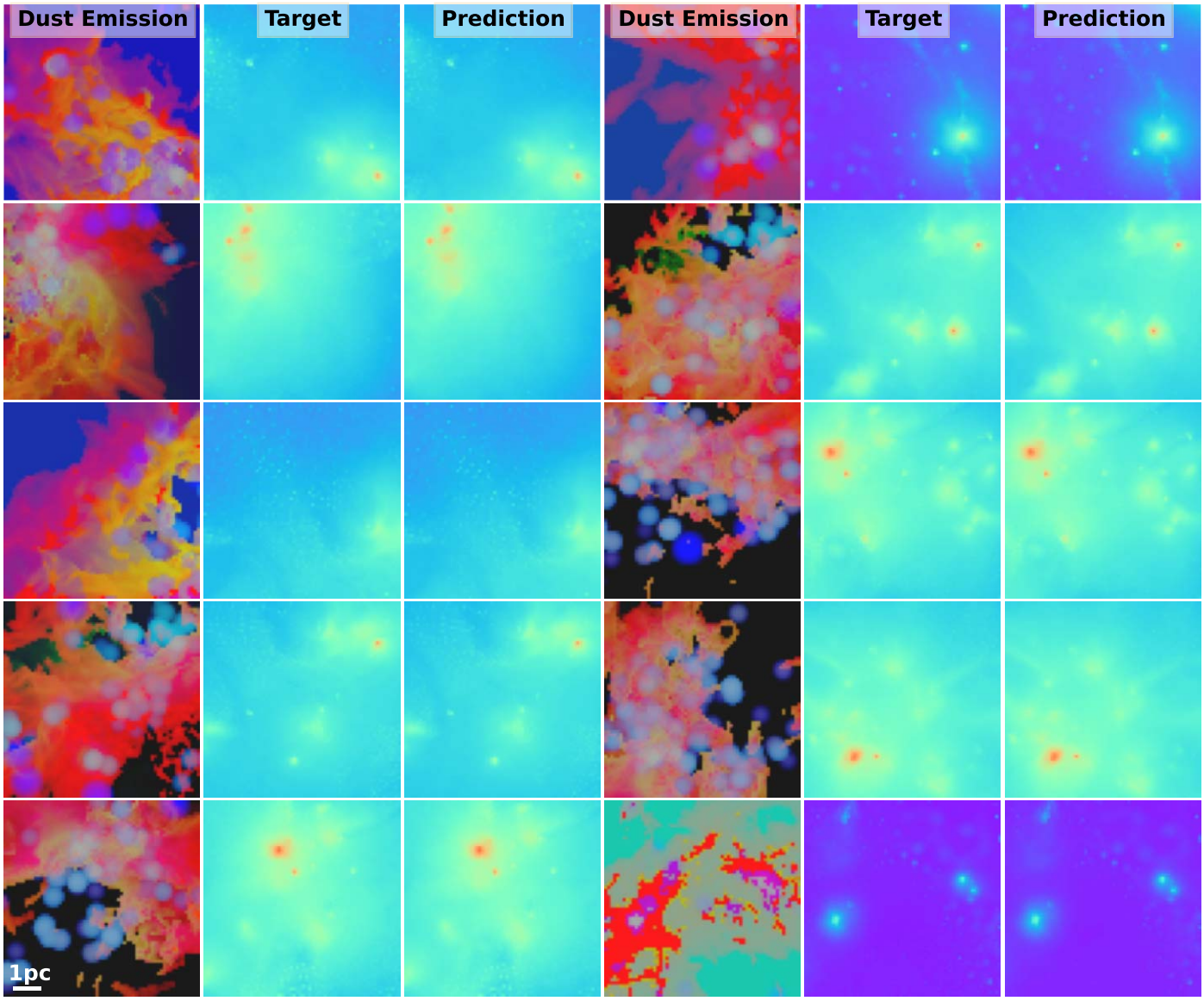

Figure 4. Predicted radiation field generated by the diffusion model (third and sixth columns), along with the corresponding three-band dust emission at 4.5 (blue), 24 (green), and 250 (red) μm (first and fourth columns) and the ground-truth radiation field (second and fifth columns).

thus provide a more realistic assessment of the prediction accuracy of the model applied to observations.

3.2.1. Different Dust Models

First, we evaluate the diffusion model's performance using synthetic dust images generated with alternative dust models, distinct from those used in the training set. It is important to note that the simulation data employed for this evaluation are identical to those used for generating the standard training and testing data sets. Therefore, the primary difference between the test data in this assessment and the standard training data lies in the selection of dust models. We consider two extreme scenarios, namely, the pure K17 model (Koepferl et al. 2017) and the pure HD23 model (Hensley & Draine 2023).

Figure 7 illustrates the correlation between the predictions of the diffusion model and the actual ground-truth values of the radiation fields in this evaluation. The histogram shows a strong alignment between the diffusion model's predictions and the actual radiation field values. The deviation between the true and predicted values is within a factor of 0.2, slightly larger than that observed in the fiducial test set described in Section 3.1. This suggests that the diffusion model can make robust predictions even when applied to the same sequence of MHD simulations with different dust model setups. Hence, the choice of a different dust model does not significantly impact the performance of the diffusion model during training and prediction.

3.2.2. Higher ISRF

Next, we assess the diffusion model's performance on new simulations characterized by significantly higher ISRF values. These simulations involve boosting the ISRF by factors of 10 and 100, resulting in ISRF intensities of $G_0 = 17$ and 170, respectively. Figure 8 illustrates the radiation field predicted by the diffusion model on these simulations. Despite the large difference in the ISRF, the diffusion model still produces predictions similar to the ground truth. However, there are some discrepancies; for instance, in the third and fourth rows of

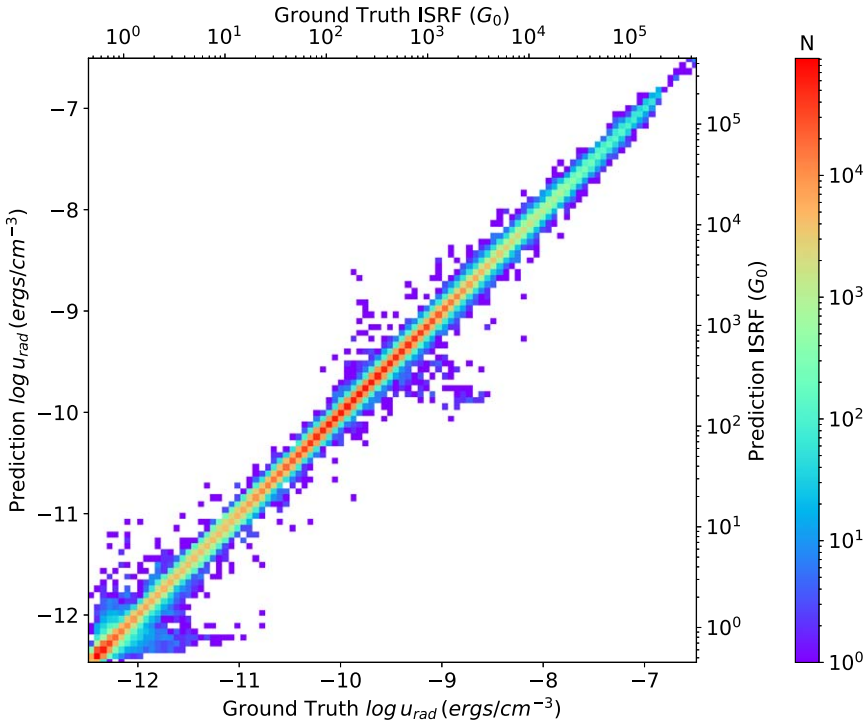

Figure 5. A 2D histogram illustrating the correlation between the predictions of the diffusion model and the ground-truth values of the radiation fields.

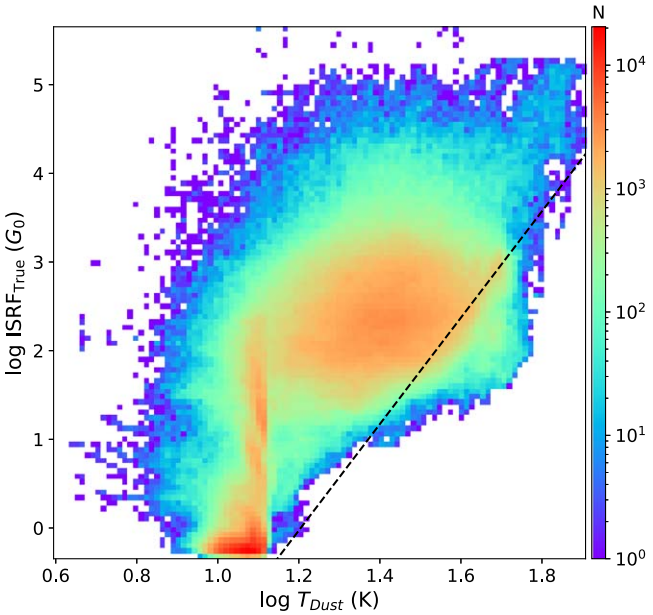

Figure 6. A 2D histogram illustrating the correlation between the true ISRF and the dust temperature in the synthetic test data. The black dashed line represents the relationship predicted by Equation (1) (Bernard et al. 2010), where the dust emissivity index β is assumed to be 2, and the incident SED is that of the unattenuated local ISRF.

the left-most three columns, the presence of dotted strong radiation regions in the actual radiation field is not accurately recovered by the diffusion model. These spots are not traced by any band of the dust emission, which explains why the diffusion model may fail to recover them.

Figure 9 presents a 2D histogram depicting the correlation between the diffusion model's predictions and the ground-truth values of the radiation fields for simulations with ISRF intensities of $G_0 = 17$ and 170. The diffusion model continues to do well, albeit returning predictions with a systematic offset. For instance, the offset between the diffusion model's predictions and the ground-truth values for the 10 times higher ISRF is approximately 0.25 dex, corresponding to an underestimation factor of 1.8. Similarly, the offset for the 100 times higher ISRF is about 0.43 dex, equivalent to an underestimation factor of 2.7. Nevertheless, the relative ISRF intensity is well constrained, as the predictions and ground-truth values still exhibit a logarithmic-linear correlation with a dispersion of 0.5. Consequently, we conclude that the diffusion model is capable of providing a reasonably accurate estimation of the radiation field even when the true field is orders of magnitude different than that of the training set. However, if a more precise estimation of the radiation field in extremely high ISRF regions is desired, it is advisable to retrain the diffusion model using an appropriate synthetic data set.

3.2.3. Higher Density and Updated Heating/Cooling

Lastly, we evaluate the diffusion model's performance using a novel set of MHD simulations featuring different initial conditions. These simulations involve driving turbulence for two crossing times as described in Lane et al. (2022), resulting in elevated gas density within the molecular cloud and well-developed turbulence throughout. In addition, these new simulations incorporate an updated radiative cooling and heating scheme utilizing the cooling module shared with the FIRE-3 simulations (Hopkins et al. 2023). In contrast, the fiducial simulations used for training relied on a simpler fitting function based on tabulated CLOUDY results (Ferland et al. 1998) accounting for local density, temperature, and metallicity. The updated MHD simulation applied in this assessment offers a more detailed representation of the heating and cooling processes, encompassing all major molecular, atomic, nebular, and continuum interactions, to better capture the thermal state

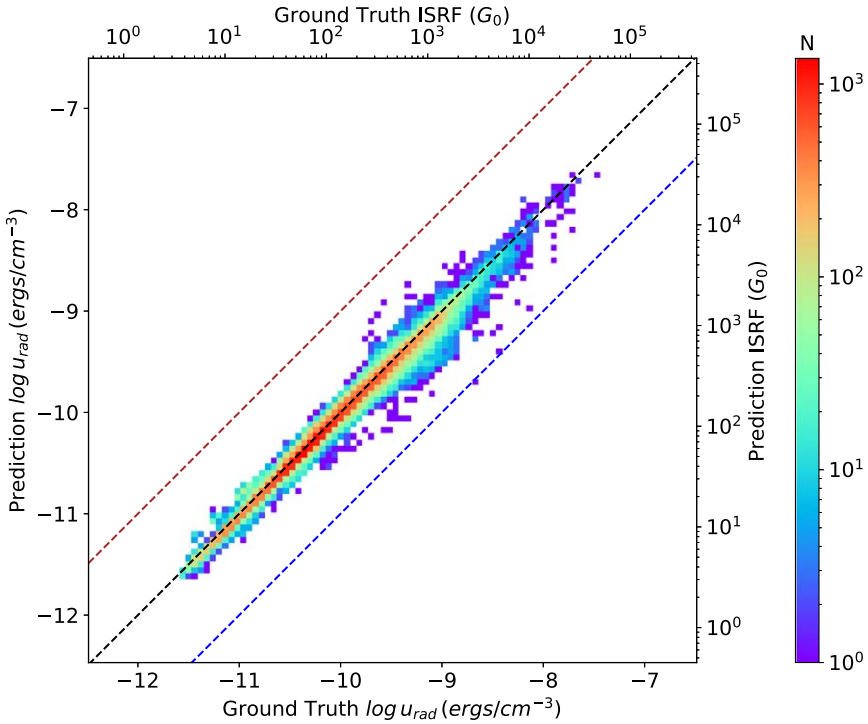

Figure 7. Similar to Figure 5 but applied to synthetic dust images generated using different dust models. The black dotted line represents the one-to-one line, which represents perfect prediction. The blue dotted line represents the 10-to-one line, indicating underestimation by a factor of 10. The brown dotted line represents the one-to-10 line, indicating overestimation by a factor of 10.

of the cold ISM (Hopkins et al. 2023). This fresh batch of simulations allows us to assess the diffusion model's performance under extreme out-of-distribution conditions.

Figure 10 displays the radiation field predictions generated by the diffusion model for these updated simulations. Despite significant differences in initial conditions and heating/cooling approaches, the diffusion model still generates predictions that closely resemble the ground truth, albeit with some discernible variations. Notably, the global background ISRF values predicted by the diffusion model are notably elevated compared to the ground truth.

To more precisely assess this divergence, we present a 2D histogram in Figure 11, illustrating the correlation between the diffusion model's predictions and the actual radiation field values for these fresh simulations. The diffusion model still performs reasonably well but exhibits a systematic offset and some variability in its predictions. It is worth noting that in these new simulations, the diffusion model appears to consistently overestimate the ISRF by approximately a factor of 3. Moreover, the dispersion in the predictions is approximately a factor of 2.

It is possible that the updated heating and cooling methods and/or the increased density within the clumps and cores in the new simulations systematically lead to a decrease in the ISRF values. This is evident from the fact that the highest ground-truth ISRF value in the new simulations is considerably smaller than that in the fiducial simulations, as observed in Figures 5 and 7.

Consequently, it is crucial to stress that accurate ISRF predictions in a real molecular cloud require an appropriate training data set reflecting the specific physical conditions of that cloud. One should exercise caution when interpreting machine-learning model predictions, especially regarding their absolute values. However, the diffusion model is capable of correctly capturing relative intensity variations across various out-of-distribution data sets. This capability provides a promising avenue for assessing the relative ISRF strengths within observed molecular clouds.

3.3. Testing on MonR2

In this section, we employ our diffusion model to analyze the actual dust observations in MonR2. The input for the diffusion model consists of three-band dust observations: 4.5, 24, and 250 μm. To ensure consistency in physical scales, we convolve the MonR2 dust observation to a similar physical resolution as our training data. Due to the larger size of the MonR2 dust map in terms of pixel count on both dimensions and the fixed image size requirement of the diffusion model (64×64), we employ a strategy that involves cropping the large map into smaller postage stamps with dimensions of 64×64 and a step size of 2 pixels. After the prediction phase, these postage stamps are combined by averaging the predictions for each pixel, resulting in the reconstruction of the original large map. Figure 12 presents the diffusion model's prediction of the radiation field. The regions of strong radiation fields predominantly align with areas of intense dust emission, which aligns with our intuitive understanding that dust is most heated in regions with relatively strong radiation fields. Notably, there is some blue dotted emission that is primarily highlighted in the 4.5 μm band. These bright dots likely represent foreground and/or background stars that are not associated with MonR2. The diffusion model's radiation field prediction appears to successfully exclude these contaminants.

Our findings demonstrate that the average projected line-of-sight ISRF in MonR2 is notably higher than the fiducial value of 1 G_0. This can be attributed to several factors. First, MonR2 is an active star-forming region where the radiation field is

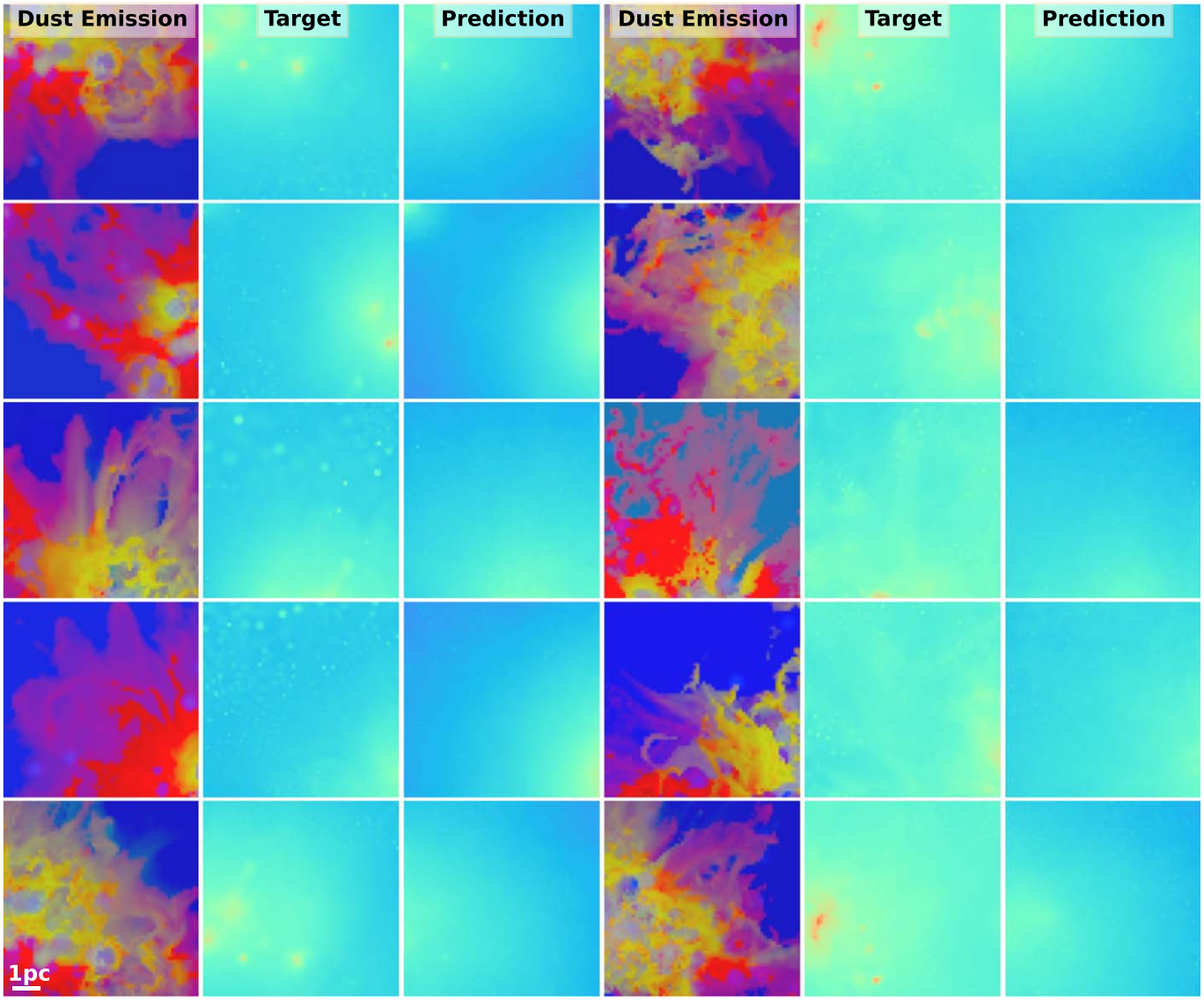

Figure 8. Predicted radiation field generated by the diffusion model, along with the corresponding three-band dust emission and ground-truth radiation field. The first three columns correspond to new simulations with an ISRF of $G_0 = 17$, while the last three columns represent simulations with an ISRF of $G_0 = 170$.

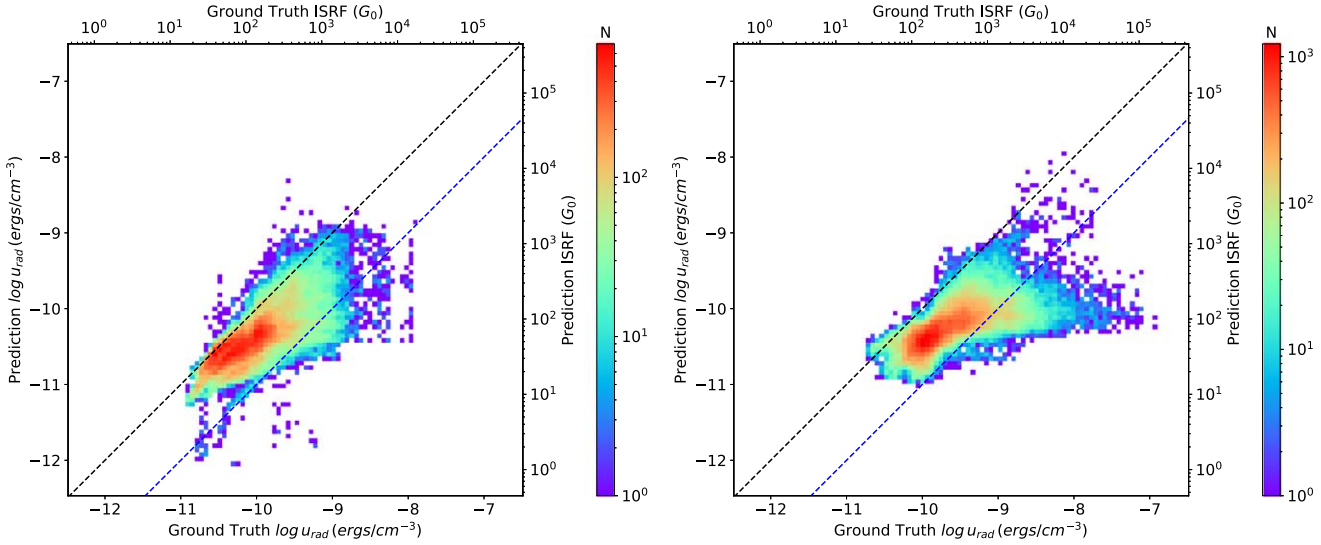

Figure 9. Similar to Figure 5 but specifically for simulations with an ISRF of $G_0 = 17$ (left panel) and 170 (right panel). The black dotted line represents the one-to-one line, which represents perfect prediction. The blue dotted line represents the 10-to-one line, indicating underestimation by a factor of 10.

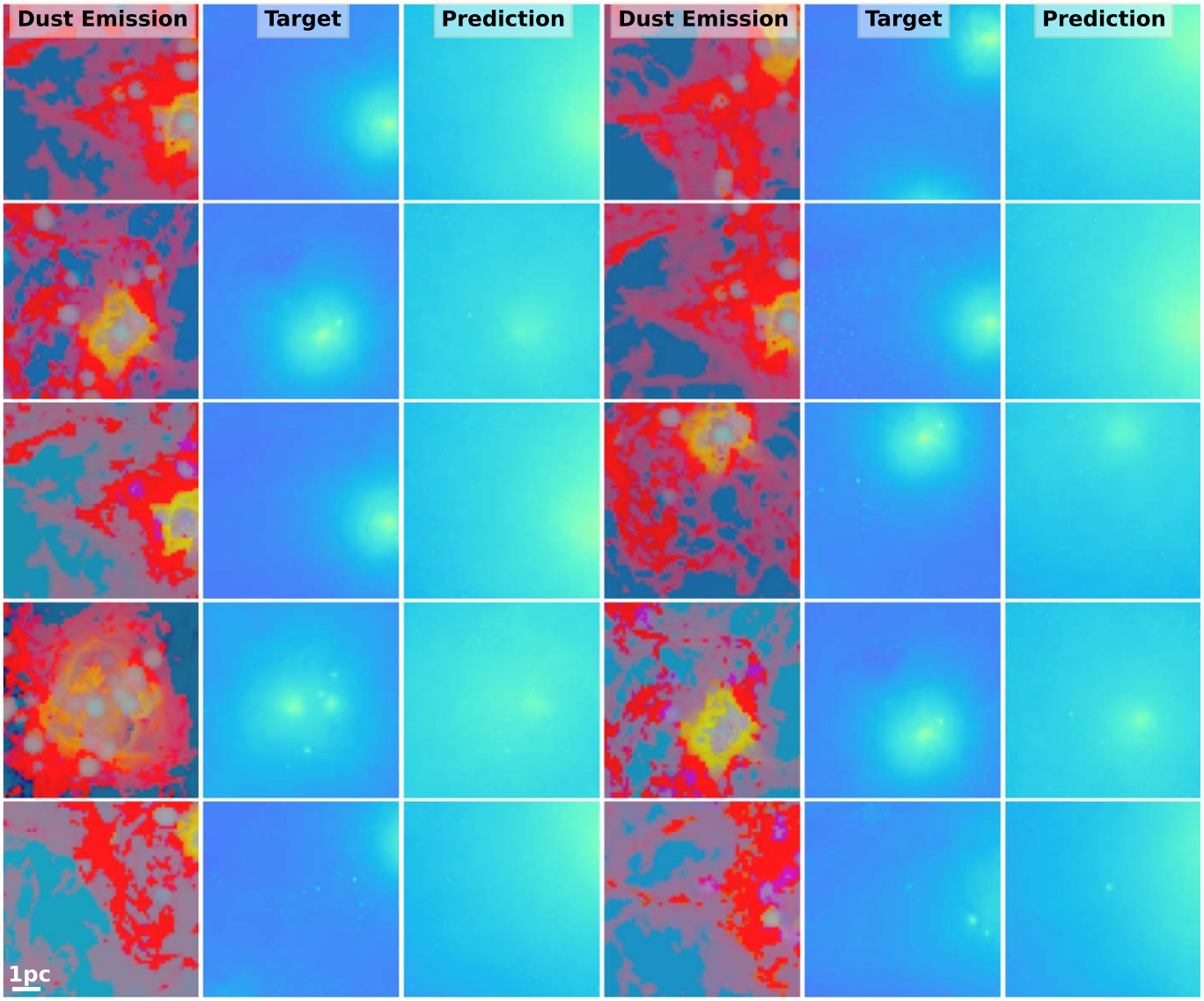

Figure 10. Predicted radiation field produced by the diffusion model alongside the associated three-band dust emission and the actual radiation field for new simulations. These simulations incorporate updated heating and cooling treatments and experience two crossing times of turbulent driving, leading to well-developed turbulence and increased gas density before self-gravity is turned on.

dominated by forming stars, leading to a significant increase in the level of ISRF. Additionally, our predicted ISRF is averaged along the line of sight into the molecular cloud without being extincted by dust, providing a more accurate estimation of the actual impact of radiation feedback across the cloud. This information is crucial for further analyses of molecular clouds, including investigating the influence of radiation feedback on the core mass function or variation of turbulent properties.

We next perform statistical analyses to investigate the correlation between the predicted ISRF and dust emission. Figure 13 presents 2D histograms illustrating this correlation at 4.5, 24, and 250 μm in MonR2. The dust emission at 4.5 μm does not exhibit a clear overall trend with the predicted ISRF. The presence of numerous blue dots, likely foreground and/or background stars unrelated to MonR2, creates a branch in the middle of the 2D histogram where the dust emission increases while the ISRF remains relatively constant. Similarly, no distinct trend is observed between the dust emission at 24 μm and the predicted ISRF. However, a positive correlation is evident between the dust emission at 250 μm and the predicted ISRF. For comparison, we investigate the correlation between the predicted ISRF and dust emission in the synthetic test data, as detailed in Appendix C. We observe a similar positive trend between the dust emission at 250 μm and the predicted ISRF in the test data.

Typically, longer-wavelength emission, such as observed by Herschel at 160, 250, 350, and 500 μm, is commonly used to estimate the dust column density and temperature. The dust temperature, in turn, can be used to estimate the radiation field, as shown in Equation 1. However, as discussed in Section 3.1 and shown in Figure 6, there is only a limited correlation between the ISRF and the dust temperature in the synthetic test data. Our study extends beyond these longer wavelengths to include the analysis of shorter-wavelength emission. By considering this broader wavelength range, we obtain a more accurate estimation of the stellar radiative feedback and dust emission.

Finally, we investigate the relationship between the predicted ISRF, the column density, and the dust temperature utilizing the column density and dust temperature maps derived by

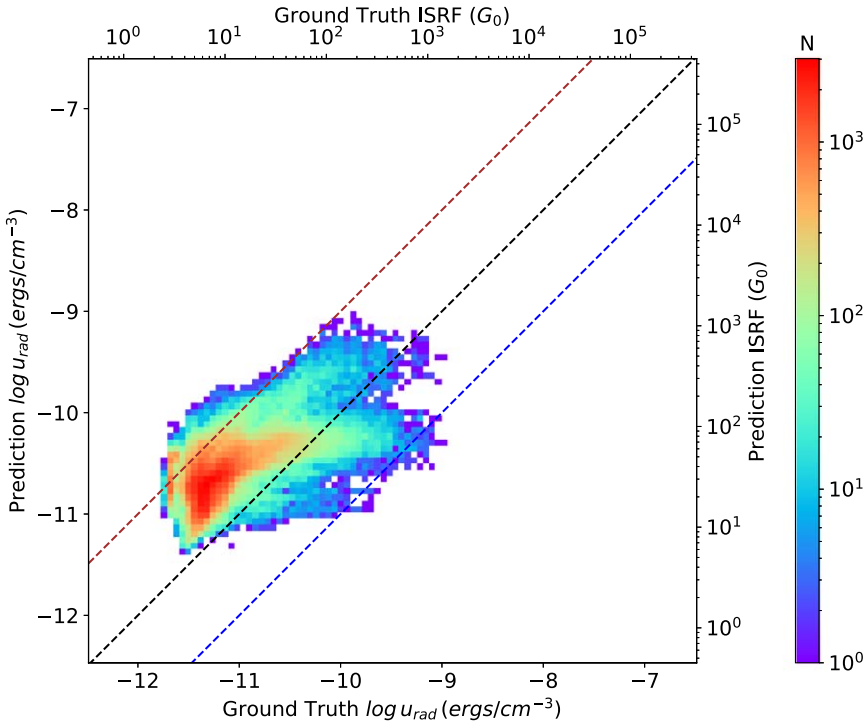

Figure 11. Similar to Figure 5 but applied to synthetic dust images generated from new simulations with updated heating and cooling treatments, as well as two crossing times of turbulent driving. The black dotted line signifies the one-to-one line, indicating perfect predictions. The blue dotted line signifies the 10-to-one line, suggesting underestimation by a factor of 10. The brown dotted line represents the one-to-10 line, indicating overestimation by a factor of 10.

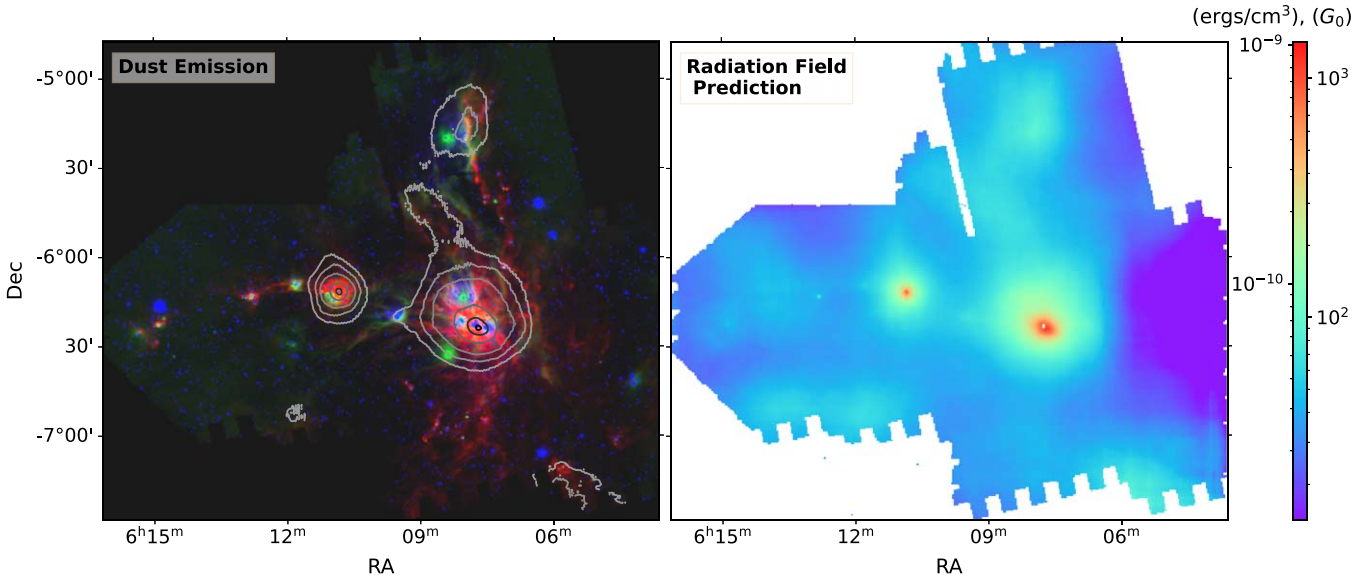

Figure 12. Three-band dust emission at 4.5 (blue), 24 (green), and 250 (red) μm in MonR2 (left panel) alongside the radiation field predicted by the diffusion model (right panel). The contour lines overlaid on the dust emission maps represent the intensity of the radiation field predicted by the diffusion model.

Pokhrel et al. (2016). Figure 14 showcases the column density and dust temperature maps of MonR2. The correlation between the predicted ISRF and the column density, as well as the dust temperature, appears to be limited. While certain regions of strong ISRF coincide with areas of high column density and dust temperature, this relationship is not consistent. Some regions with high column density and/or dust temperature do not exhibit a strong ISRF. Figure 15 displays 2D histograms illustrating the correlation in MonR2. Notably, we do not observe a clear trend between the ISRF and dust temperature, in contrast to typical modeling assumptions (e.g., Bernard et al. 2010). Although a positive correlation can be discerned when the dust temperature exceeds 20 K (log $T = 1.3$), it is accompanied by significant scatter.

It is important to highlight that the black line, representing the ISRF inferred from the graybody dust temperature, is significantly offset from the DDPM-predicted ISRF values. This discrepancy may suggest that radiation from embedded stars is highly attenuated, resulting in much cooler dust temperatures. Another possibility is that the dust consists of

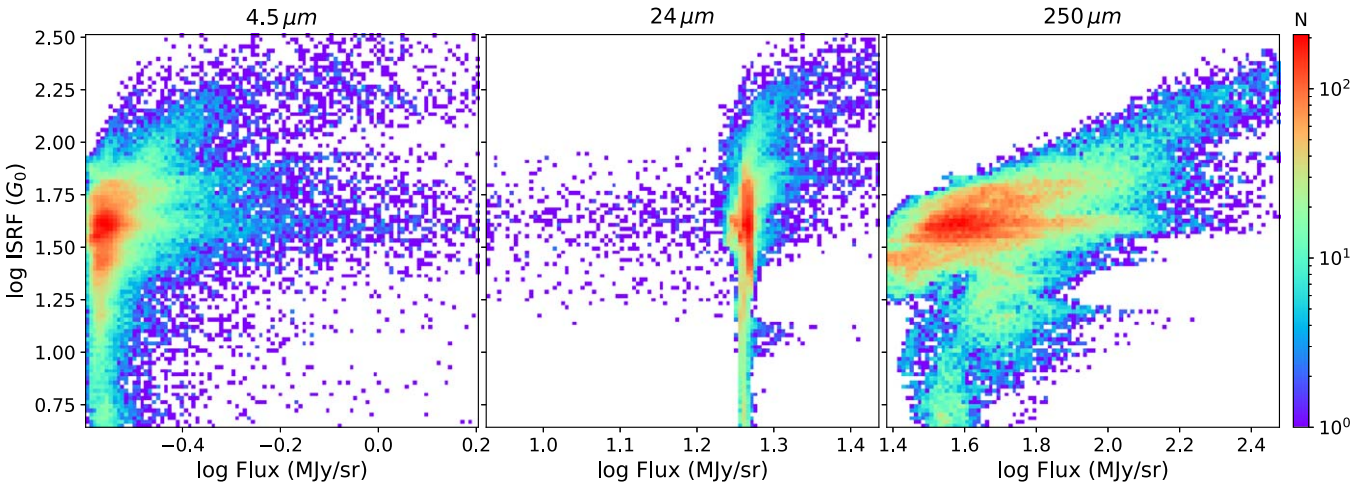

Figure 13. The 2D histograms illustrating the correlation between the predicted ISRF and the dust emission intensity (4.5 μm on the left, 24 μm in the middle, and 250 μm on the right) in MonR2.

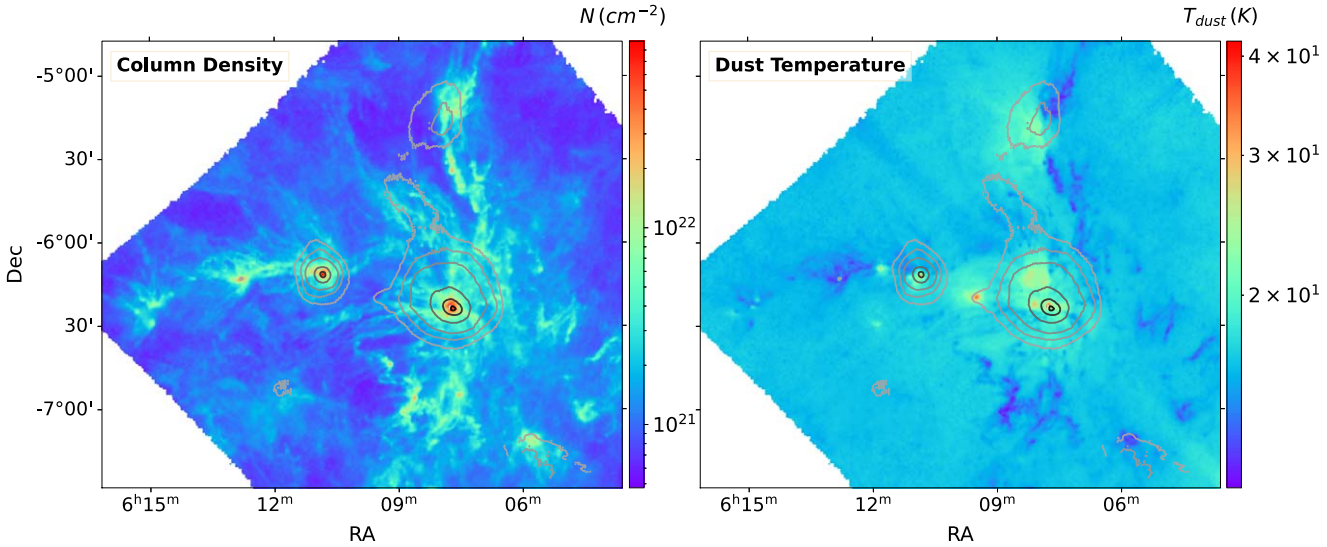

Figure 14. Column density (left) and dust temperature (right) maps derived by Pokhrel et al. (2016). The contour lines represent the intensity of the radiation field predicted by the diffusion model.

multiple temperature components, with the colder components dominating the emission in the Herschel band used to derive this temperature map. Similarly, no distinct pattern emerges between the predicted ISRF and the column density. These findings suggest that the dust emission at 250 μm is influenced by factors beyond just column density and dust temperature, including the presence of radiation.

4. Conclusions

We produced synthetic dust observations of MHD simulations from the STARFORGE project that incorporate various physical processes to simulate star formation and GMC evolution. Using these synthetic observations, we trained deep-learning diffusion models to estimate the radiation field strength based on three-band dust emission at 4.5, 24, and 250 μm. We evaluated the performance of the diffusion model on both synthetic test samples and real observational data. The key findings of our study are summarized as follows.

1. We performed radiative transfer simulations with various treatments for the spectra of stellar sources, resulting in the generation of 9750 synthetic dust emission maps. We find that the agreement with the observed dust emission is very sensitive to the assumed dust model and show that the Hensley & Draine (2023) model for diffuse gas combined with the Koepferl et al. (2017) model for densities above 10^5 cm^{-3} provides a good representation of the MonR2 dust emission.
2. We utilized deep-learning diffusion models to estimate the strength of the radiation field and assessed its performance on the test set. The diffusion model successfully reconstructed the radiation field strength at the pixel level, generally recovering the true value within 10%.
3. We found that the relationship between ISRF and dust temperature exhibits a high degree of scatter, such that a simple graybody model for dust emission does not accurately predict the radiation field.

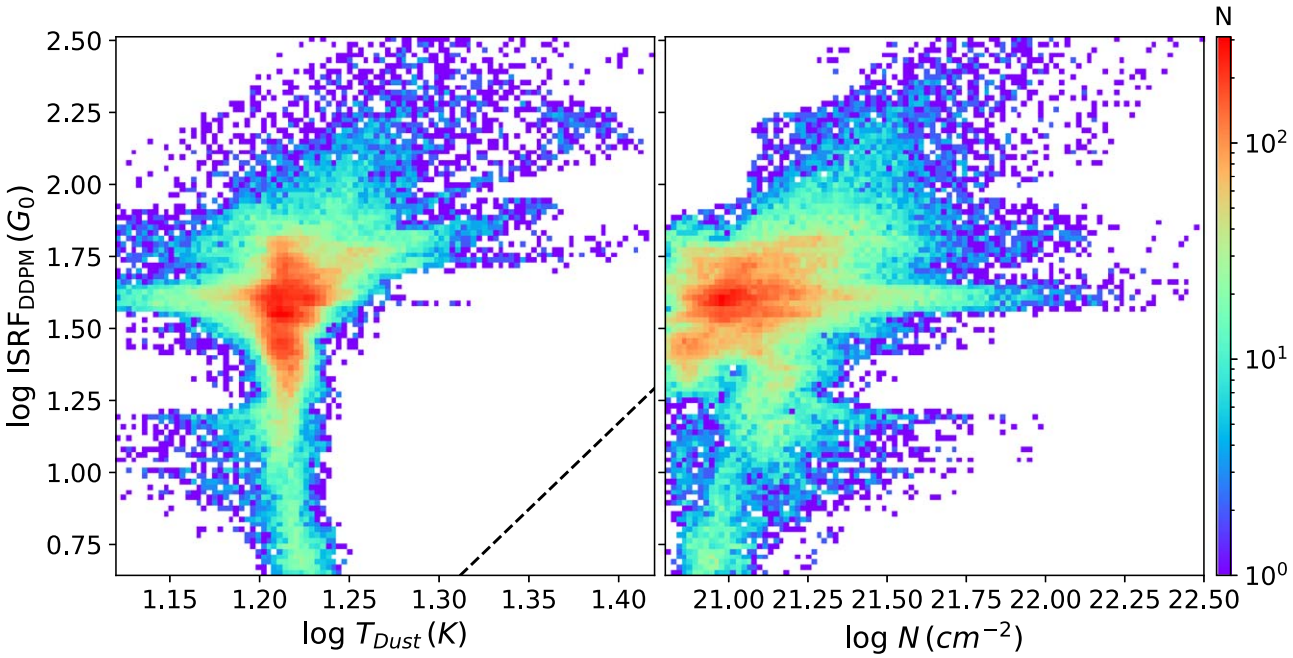

Figure 15. The 2D histograms illustrating the correlation between the predicted ISRF and the dust temperature (left panel) and the column density (right panel) in MonR2. The black dashed line in the left panel represents the predicted relation between the ISRF and dust temperature given in Equation (1).

4. We evaluated the performance of the diffusion model using synthetic dust images created with different dust models than those employed in the training set. The results indicate that the diffusion model can accurately predict the ISRF, with errors within a 20% range. This suggests that the diffusion model is not overly sensitive to our choice of dust model and can provide reliable predictions even when applied to MHD simulations with varying dust model configurations.
5. We assessed the performance of the diffusion model on new MHD simulations featuring an ISRF that is 10 and 100 times higher than that of the fiducial simulations. The diffusion model was still able to predict the ISRF reasonably accurately, although there was a systematic underestimation factor of 1.8 and 2.7 for the 10 and 100 times higher ISRF, respectively.
6. We assessed the performance of the diffusion model using new MHD simulations featuring updated heating/cooling and initial turbulent driving. The model performed satisfactorily but consistently overestimated the ISRF by a factor of 3, with a dispersion of approximately a factor of 2. This overestimation is likely due to the updated heating/cooling treatments, which systematically cause lower ISRF values in the simulations relative to simulations in the fiducial training set.
7. The evaluation of the out-of-distribution data set underscores the resilience of the diffusion model in predicting the relative ISRF levels within a single molecular cloud. While there are systematic offsets in the absolute ISRF values, the relative intensity of the ISRF is accurately estimated with a dispersion of up to a factor of 2.
8. We employed the diffusion model to predict the radiation field in MonR2 using observed dust emission. The diffusion model successfully captures the locations of intense radiation field regions, which corresponded to areas with high dust emission. We find a positive correlation between the predicted ISRF and the dust emission at 250 μm with a large degree of scatter.

Although the model performs well overall, we stress that the test simulations, which represent out-of-distribution data, produce significantly less precise model predictions. This suggests that the uncertainties associated with the predicted ISRF represent upper limits on the accuracy of the ISRF predicted from observational data, as, by definition, our training set is out of distribution compared to actual observations. Therefore, it is important to adopt an appropriate training data set that reflects the particular physical conditions of the targeted molecular cloud as accurately as possible to ensure the most precise ISRF prediction.

In future work, we plan to extend the application of the diffusion model to additional archived dust observations of nearby molecular clouds, as well as to nearby galaxies. This approach will allow us to study the impact of radiation fields on molecular clouds and star formation in a broader context.

Acknowledgments

We would like to express our gratitude to the anonymous referee for the invaluable suggestions, particularly those pertaining to the assessment of out-of-distribution data. D.X. acknowledges support from the Virginia Initiative on Cosmic Origins (VICO). S.S.R.O. and R.G. acknowledge funding support for this work from NSF AAG grants 2107340 and 2107705. S.S.R.O. acknowledges support by NSF through CAREER award 1748571, AST-2107340, and AST-2107942; NASA through grants 80NSSC20K0507 and 80NSSC23K0476; and the Oden Institute through a Moncrief Grand Challenge award. The authors acknowledge Research Computing at the University of Virginia for providing computational resources and technical support that have contributed to the results reported within this publication.

Appendix A
Star Categorization in Radiative Transfer

In this section, we provide an example of categorizing stars based on their effective temperature in radiative transfer. Due to computational limitations, it is not feasible to perform radiative transfer for each individual star in the simulation. Instead, we employ a binning approach to group stars into four categories based on their effective temperature. Figure 16 illustrates the projected stellar radiation density and corresponding SEDs for a snapshot of simulations at 4.5 Myr without jets, as depicted in the third row of Figure 1. The stellar field is represented by bloblike structures deposited onto the grid with an FWHM of 3 pixels. The SEDs for each star category are displayed, including the blackbody SED and the YSO SED with disks from Robitaille (2017). Notably, the input YSO SEDs exhibit a significant excess of infrared emission due to radiative emission by an assumed circumstellar disk.

Appendix B
Exploration of Different Dust Models

In this section, we examine different cutoffs on gas number densities for selecting dust models and explore the impact of different dust models on the synthetic observations. Our primary dust model is a hybrid approach combining the K17 (Koepferl et al. 2017) model for $n > 10^5$ cm^{-3} and the HD23 (Hensley & Draine 2023) model for $n < 10^5$ cm^{-3}. We vary the cutoff density, $\rho_{\rm cut}$, from 1 to 10^7 cm^{-3}, as well as consider a pure K17 model (i.e., $\rho_{\rm cut} = 0$) and a pure HD23 model (i.e., $\rho_{\rm cut} = \infty$). Additionally, we examine the performance of a traditional dust model, DL84 (Draine & Lee 1984), on the synthetic observations.

Figures 17 and 18 depict the synthetic images in three bands (4.5, 24, and 250 μm) and the corresponding SEDs obtained using different cutoffs on gas number densities and different dust models. The overall appearance of the synthetic images in the three bands remains similar; however, the relative intensity of the bands varies with different density cutoffs. The adoption

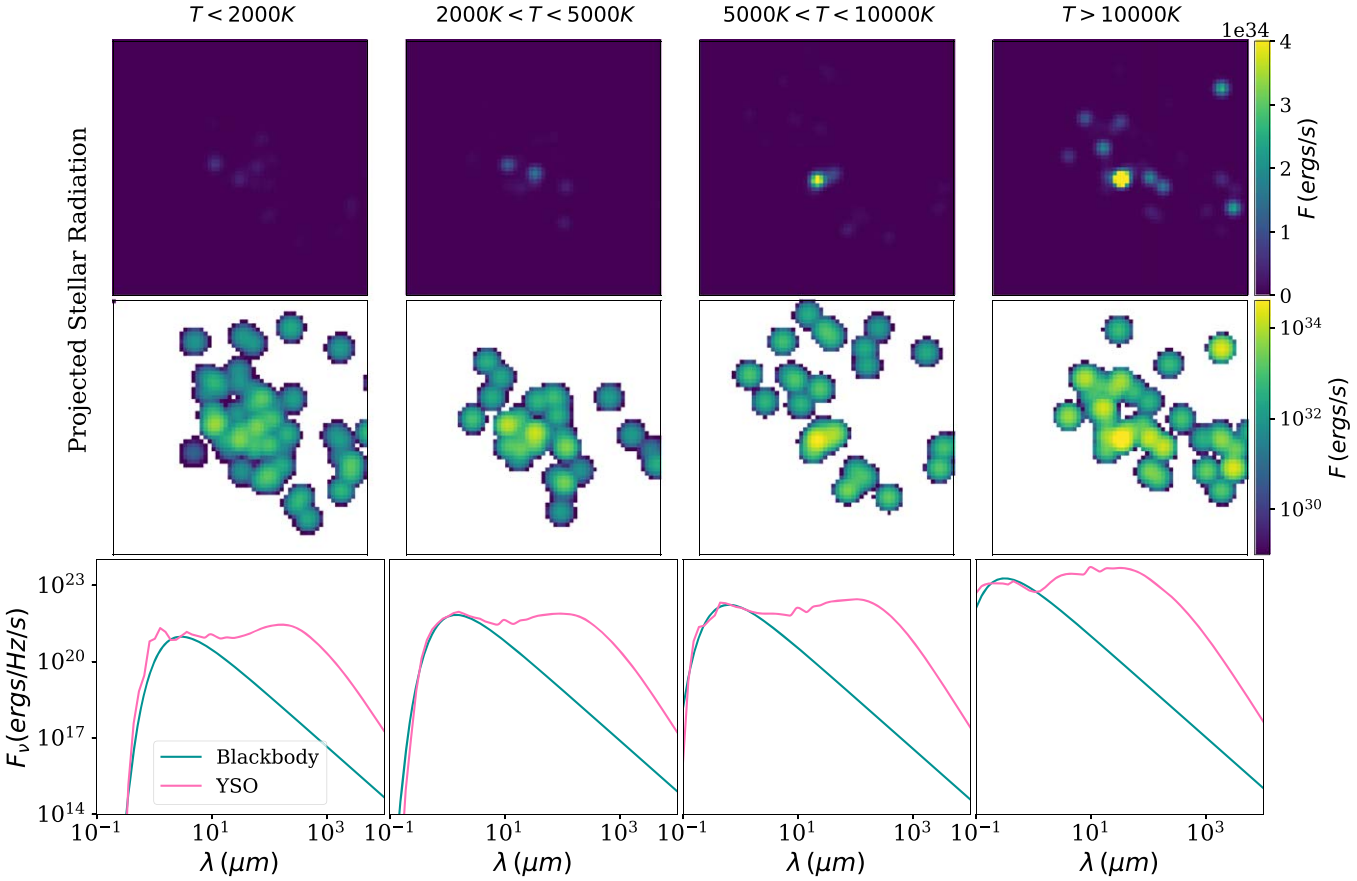

Figure 16. Projected stellar radiation density and corresponding SEDs of different categories for a snapshot of simulations at 4.5 Myr without jets (third row of Figure 1).

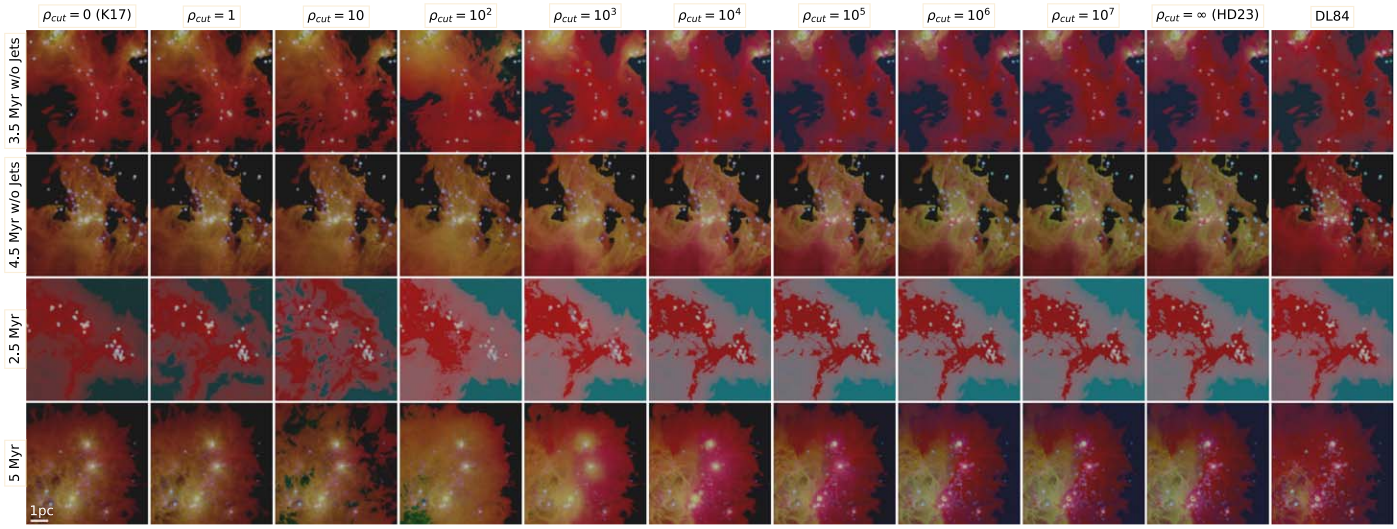

Figure 17. Synthetic images at three different wavelengths (4.5, 24, and 250 μm) generated by employing different cutoffs ($\rho_{\rm cut}$) on gas number densities when selecting dust models and different dust models in the radiative transfer for different simulation snapshots.

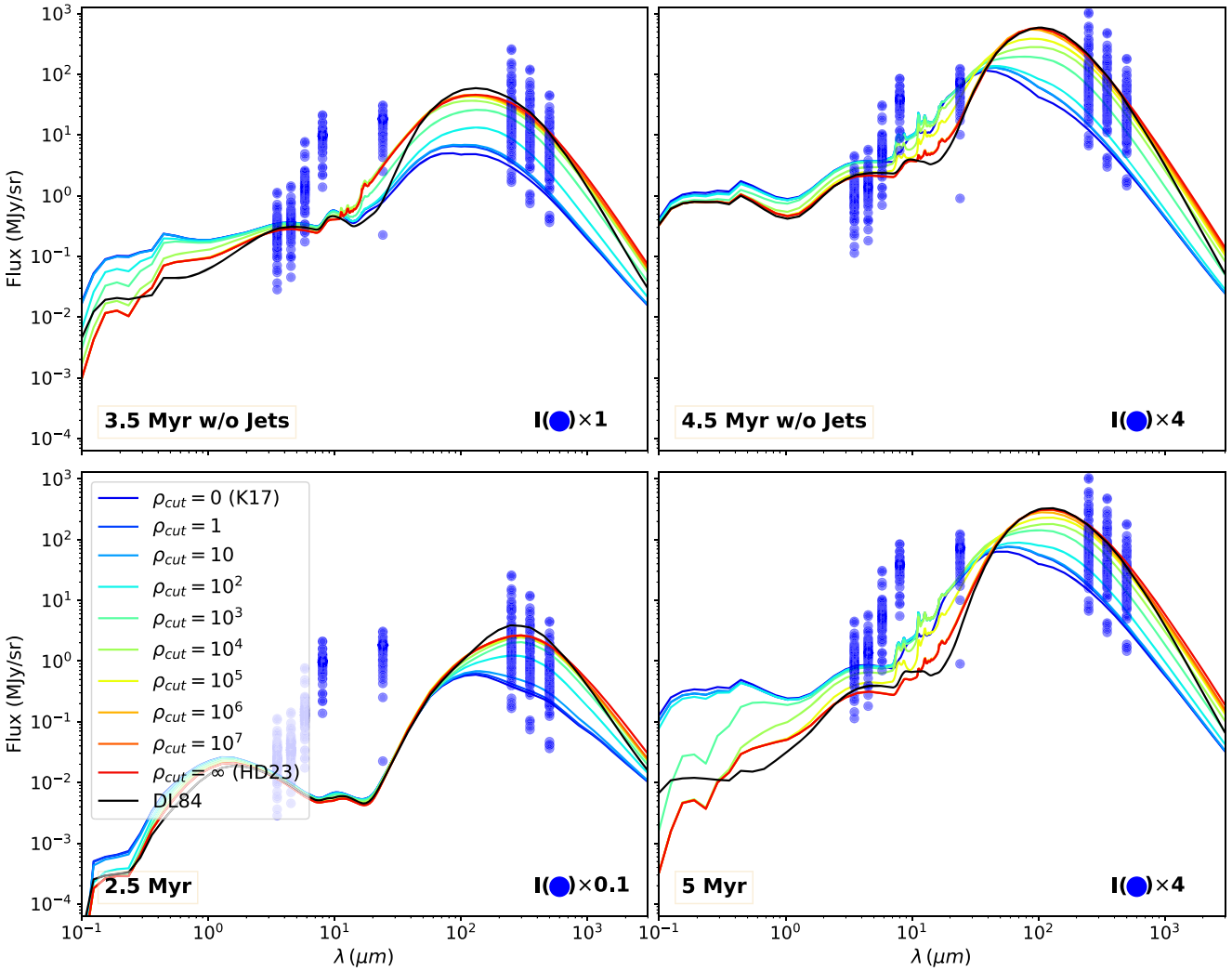

Figure 18. The SEDs obtained by employing different cutoffs on gas number densities when selecting dust models and different dust models in the radiative transfer for different simulation snapshots. The blue dots represent the observed SEDs in MonR2, which have been rescaled by specific factors, as indicated in the lower right corner.

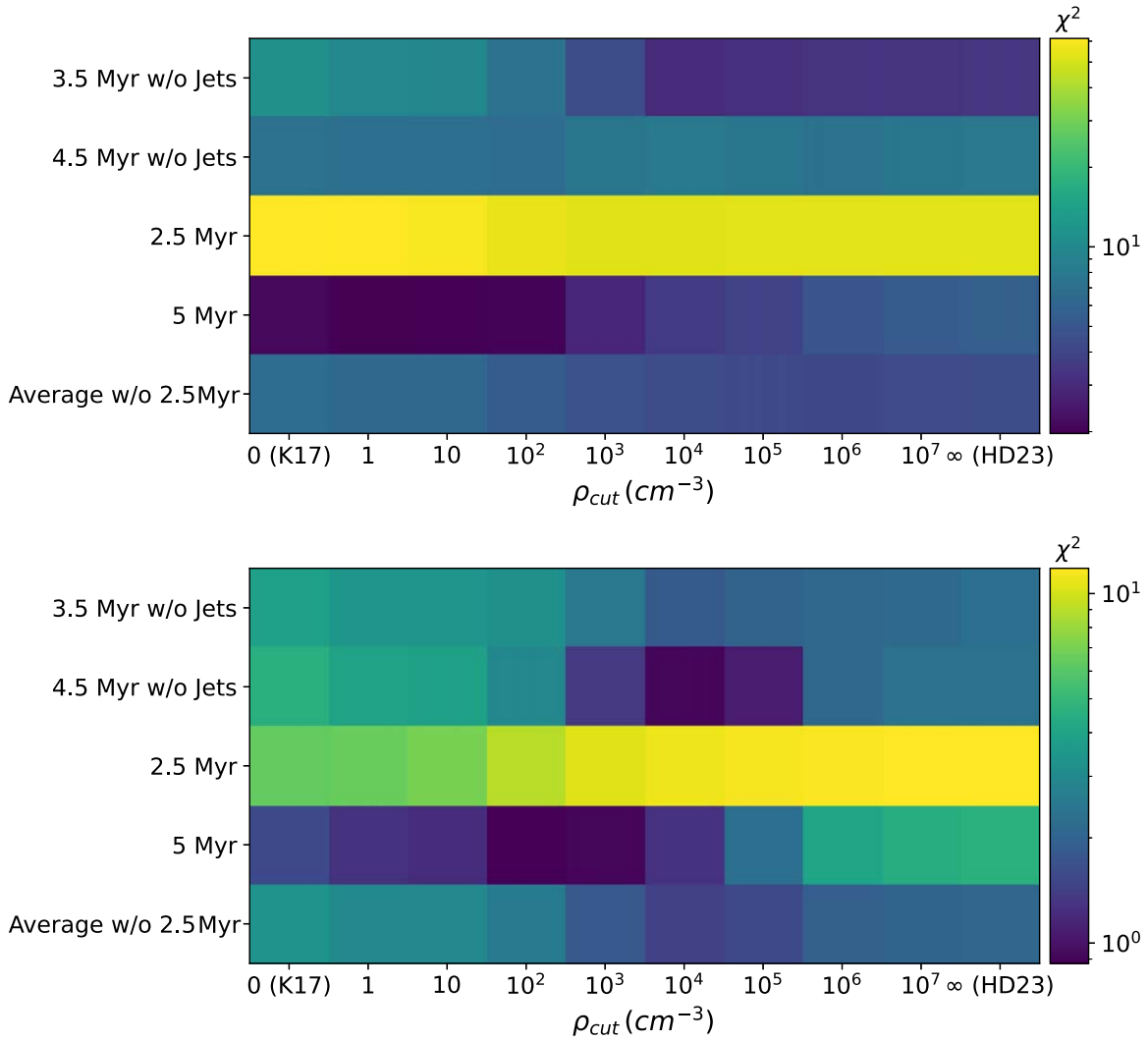

Figure 19. The χ^2 values calculated between the synthetic and observed SEDs across various gas number density cutoffs during dust model selection and different evolutionary stages in various simulations. The upper panel displays the raw χ^2 values calculated between the synthetic and observed SEDs. In the lower panel, we compute the χ^2 values while incorporating a free scaling parameter during the calculation.

of the K17 model results in a more yellowish color, while the HD23 model yields a more reddish color. This discrepancy indicates that the synthetic dust emission using the K17 model emits fewer long-wavelength photons compared to the HD23 model. This distinction is further evident in the SEDs, where the synthetic dust emission utilizing the K17 model exhibits weaker emission at long wavelengths but stronger emission at short wavelengths in comparison to the HD23 model. When comparing these synthetic results with the observed SEDs in MonR2, it becomes apparent that the HD23 model and the combination of the K17 and HD23 models better reproduce the observed emission characteristics.

The SEDs obtained using the HD23 and DL84 models exhibit similarities, but there is a notable difference. The DL84 model fails to reproduce the PAH feature around 10 μm.

To quantitatively evaluate the discrepancies between synthetic and observed SEDs, we provide the χ^2 values in Figure 19. We utilize two strategies for computing these χ^2 values. One approach directly calculates the χ^2 value between the synthetic and observed SEDs. The other method involves introducing a free parameter to scale the synthetic SEDs in intensity, thereby obtaining the best fit for the observed SED shape, before computing the χ^2. We present both for reference, since they suggest slightly different preferred dust models.

It is apparent that MonR2 is not in its early evolutionary stages, as is evident from the notably higher χ^2 values for the 2.5 Myr snapshots compared to other stages. Moreover, the χ^2 trends across different $\rho_{\rm cut}$ values exhibit variations depending on the evolutionary stage and simulation. When averaging the χ^2 values across simulations, excluding the early evolution at 2.5 Myr, we find that $\rho_{\rm cut} = 10^6$ cm^{-3} provides the best fit for the raw χ^2, while $\rho_{\rm cut} = 10^4$ cm^{-3} yields the best results for the scaled χ^2. We acknowledge that the choice of $\rho_{\rm cut}$ may appear somewhat arbitrary, since it relies on SED comparisons, which highlight the absence of a single synthetic SED that perfectly matches the observed SEDs in MonR2. By considering both methods for calculating the χ^2 values, we opt for $\rho_{\rm cut} = 10^5$ cm^{-3}. This choice can also be regarded as empirical, representing the observed distinction between diffuse and dense gas.

Appendix C
Correlation between the ISRF and Dust Emission in Synthetic Test Data

We analyze the relationship between the ISRF and dust emission intensity in Figure 20. Similar to Figure 13, no distinct correlation occurs between the dust emission at 4.5 μm and the ISRF. A weak positive correlation is apparent between the dust emission at 24 μm and the ISRF. A clear positive correlation occurs between the dust emission at 250 μm and the ISRF. This indicates that our analysis provides independent and complementary information to the typical analysis of the Herschel wave bands (160, 250, 350, and 500 μm) used for deriving the dust temperature. Consequently, our approach presents a new metric to quantify the physical environment within molecular clouds.

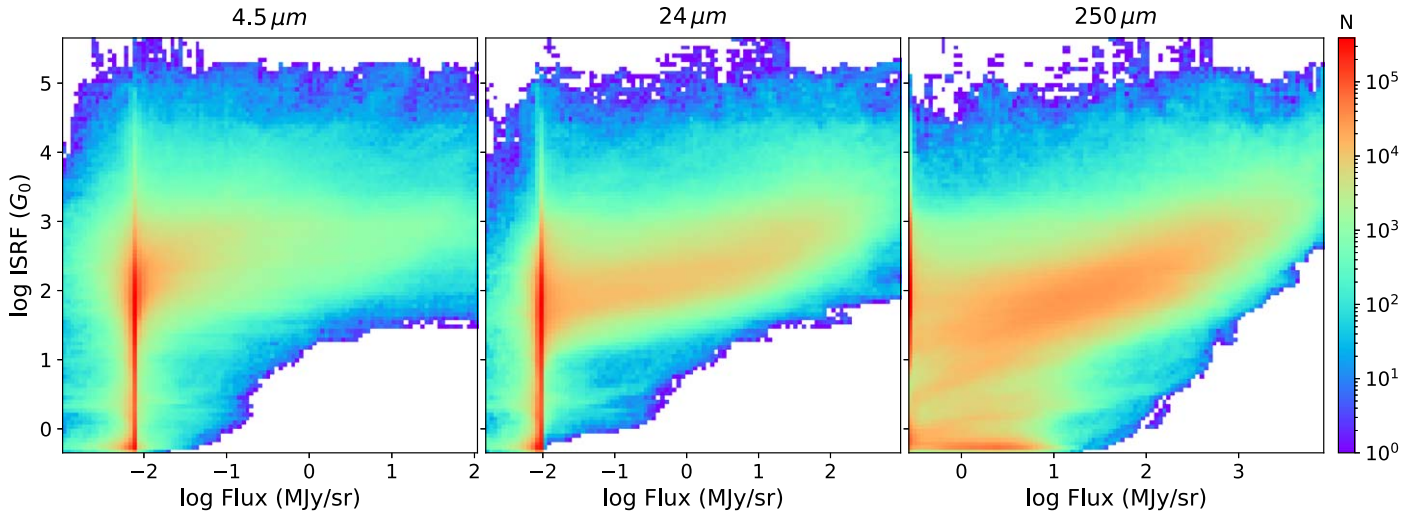

Figure 20. The 2D histograms illustrating the correlation between the ISRF and the dust emission intensity (4.5 μm on the left, 24 μm in the middle, and 250 μm on the right) in the synthetic test data.

ORCID iDs

Duo Xu https://orcid.org/0000-0001-6216-8931
Stella S. R. Offner https://orcid.org/0000-0003-1252-9916
Robert Gutermuth https://orcid.org/0000-0002-6447-899X
Michael Y. Grudić https://orcid.org/0000-0002-1655-5604
Dávid Guszejnov https://orcid.org/0000-0001-5541-3150
Philip F. Hopkins https://orcid.org/0000-0003-3729-1684

References

Arce, H. G., Shepherd, D., Gueth, F., et al. 2007, in Protostars and Planets V, ed. B. Reipurth, D. Jewitt, & K. Keil (Tucson, AZ: Univ. of Arizona Press), 245
Asensio Ramos, A., & Díaz Baso, C. J. 2019, A&A, 626, A102
Bernard, J. P., Paradis, D., Marshall, D. J., et al. 2010, A&A, 518, L88
Bisbas, T. G., Bell, T. A., Viti, S., Yates, J., & Barlow, M. J. 2012, MNRAS, 427, 2100
Churchwell, E., Watson, D. F., Povich, M. S., et al. 2007, ApJ, 670, 428
Cyganowski, C. J., Whitney, B. A., Holden, E., et al. 2008, AJ, 136, 2391
Dale, J. E., Ercolano, B., & Bonnell, I. A. 2012, MNRAS, 424, 377
Dale, J. E., Ercolano, B., & Bonnell, I. A. 2013, MNRAS, 430, 234
Draine, B. T. 1978, ApJS, 36, 595
Draine, B. T., & Lee, H. M. 1984, ApJ, 285, 89
Dullemond, C. P., Juhasz, A., Pohl, A., et al., 2012 RADMC-3D: A multi-purpose radiative transfer tool, Astrophysics Source Code Library, ascl:1202.015
Fall, S. M., Krumholz, M. R., & Matzner, C. D. 2010, ApJL, 710, L142
Fazio, G. G., Hora, J. L., Allen, L. E., et al. 2004, ApJS, 154, 10
Federrath, C. 2015, MNRAS, 450, 4035
Federrath, C., Schrön, M., Banerjee, R., & Klessen, R. S. 2014, ApJ, 790, 128
Ferland, G. J., Korista, K. T., Verner, D. A., et al. 1998, PASP, 110, 761
Foschino, S., Berné, O., & Joblin, C. 2019, A&A, 632, A84
Frank, A., Ray, T. P., Cabrit, S., et al. 2014, in Protostars and Planets VI, ed. H. Beuther et al. (Tucson, AZ: Univ. of Arizona Press), 451
Girichidis, P., Offner, S. S. R., Kritsuk, A. G., et al. 2020, SSRv, 216, 68
Griffin, M. J., Abergel, A., Abreu, A., et al. 2010, A&A, 518, L3
Grudić, M. Y., Guszejnov, D., Hopkins, P. F., Offner, S. S. R., & Faucher-Giguère, C.-A. 2021, MNRAS, 506, 2199
Grudić, M. Y., Guszejnov, D., Offner, S. S. R., et al. 2022, MNRAS, 512, 216
Grudić, M. Y., & Hopkins, P. F. 2019, MNRAS, 488, 2970
Guszejnov, D., Grudić, M. Y., Offner, S. S. R., et al. 2022, MNRAS, 515, 4929
Hensley, B. S., & Draine, B. T. 2023, ApJ, 948, 55
Ho, J., Jain, A., & Abbeel, P. 2020, in Advances in Neural Information Processing Systems, ed. H. Larochelle et al., Vol. 33 (Red Hook, NY: Curran Associates, Inc.), 6840, https://proceedings.neurips.cc/paper/2020/file/4c5bcfec8584af0d967f1ab10179ca4b-Paper.pdf
Hopkins, P. F. 2015, MNRAS, 450, 53
Hopkins, P. F., Wetzel, A., Wheeler, C., et al. 2023, MNRAS, 519, 3154
Koepferl, C. M., Robitaille, T. P., Dale, J. E., & Biscani, F. 2017, ApJS, 233, 1
Landsman, W. B. 1993, in ASP Conf. Ser. 52, Astronomical Data Analysis Software and Systems II, ed. R. J. Hanisch, R. J. V. Brissenden, & J. Barnes (San Francisco, CA: ASP), 246
Lane, H. B., Grudić, M. Y., Guszejnov, D., et al. 2022, MNRAS, 510, 4767
Looney, L. W., Tobin, J. J., & Kwon, W. 2007, ApJL, 670, L131
Lopez, L. A., Krumholz, M. R., Bolatto, A. D., et al. 2014, ApJ, 795, 121
Mathis, J. S., Mezger, P. G., & Panagia, N. 1983, A&A, 128, 212
Matzner, C. D. 2007, ApJ, 659, 1394
Neutsch, S., Heneka, C., & Brüggen, M. 2022, MNRAS, 511, 3446
Offner, S. S. R., & Chaban, J. 2017, ApJ, 847, 104
Offner, S. S. R., Klein, R. I., McKee, C. F., & Krumholz, M. R. 2009, ApJ, 703, 131
Offner, S. S. R., Robitaille, T. P., Hansen, C. E., McKee, C. F., & Klein, R. I. 2012, ApJ, 753, 98
Peek, J. E. G., & Burkhart, B. 2019, ApJL, 882, L12
Pilbratt, G. L., Riedinger, J. R., Passvogel, T., et al. 2010, A&A, 518, L1
Planck HFI Core Team, Ade, P. A. R., Aghanim, N., et al. 2011, A&A, 536, A4
Pokhrel, R., Gutermuth, R., Ali, B., et al. 2016, MNRAS, 461, 22
Pokhrel, R., Gutermuth, R. A., Betti, S. K., et al. 2020, ApJ, 896, 60
Pound, M. W., & Wolfire, M. G. 2023, AJ, 165, 25
Rieke, G. H., Young, E. T., Engelbracht, C. W., et al. 2004, ApJS, 154, 25
Robitaille, T. P. 2017, A&A, 600, A11
Robitaille, T. P., Whitney, B. A., Indebetouw, R., & Wood, K. 2007, ApJS, 169, 328
Rombach, R., Blattmann, A., Lorenz, D., Esser, P., & Ommer, B. 2022, in IEEE/CVF Conf. on Computer Vision and Pattern Recognition (CVPR), 10684
Rosen, A. L. 2022, ApJ, 941, 202
Rosen, A. L., & Krumholz, M. R. 2020, AJ, 160, 78
Smith, M. J., Geach, J. E., Jackson, R. A., et al. 2022, MNRAS, 511, 1808
Sohl-Dickstein, J., Weiss, E., Maheswaranathan, N., & Ganguli, S. 2015, in Proc. of Machine Learning Research, Vol. 37, Proc. of the 32nd Int. Conf. on Machine Learning, ed. F. Bach & D. Blei (Lille, France: PMLR), 2256, https://proceedings.mlr.press/v37/sohl-dickstein15.html
Takami, M., Karr, J. L., Koh, H., Chen, H.-H., & Lee, H.-T. 2010, ApJ, 720, 155
Tobin, J. J., Hartmann, L., Calvet, N., & D'Alessio, P. 2008, ApJ, 679, 1364
Turk, M. J., Smith, B. D., Oishi, J. S., et al. 2011, ApJS, 192, 9
Van Oort, C. M., Xu, D., Offner, S. S. R., & Gutermuth, R. A. 2019, ApJ, 880, 83
Walch, S. K., Whitworth, A. P., Bisbas, T., Wünsch, R., & Hubber, D. 2012, MNRAS, 427, 625
Wang, P., Li, Z.-Y., Abel, T., & Nakamura, F. 2010, ApJ, 709, 27
Wang, R., Chen, Z., Luo, Q., & Wang, F. 2023, arXiv:2305.09121
Werner, M. W., Roellig, T. L., Low, F. J., et al. 2004, ApJS, 154, 1
Whitney, B. A., Wood, K., Bjorkman, J. E., & Cohen, M. 2003, ApJ, 598, 1079
Wu, J. F., & Boada, S. 2019, MNRAS, 484, 4683
Xu, D., Offner, S. S. R., Gutermuth, R., Kong, S., & Arce, H. G. 2022a, ApJ, 926, 19
Xu, D., Offner, S. S. R., Gutermuth, R., & Oort, C. V. 2020a, ApJ, 905, 172
Xu, D., Offner, S. S. R., Gutermuth, R., & Oort, C. V. 2020b, ApJ, 890, 64
Xu, D., Offner, S. S. R., Gutermuth, R., & Tan, J. C. 2022b, ApJ, 941, 81
Xu, D., Tan, J. C., Hsu, C.-J., & Zhu, Y. 2023, ApJ, 950, 146